FLUID COMPOSITION CHANGES IN CRYSTALLINE BASEMENT ROCKS FROM DUCTILE TO BRITTLE REGIMES

Irene Cantarero[a]*, Gemma Alías[a], David Cruset[a], Eloi Carola[b], Pierre Lanari[c], Anna Travé[a]

[a]Departament de Mineralogia, Petrologia i Geologia Aplicada. Facultat de Ciències de la Terra, Universitat de Barcelona (UB) C/Martí i Franqués s/n, 08028, Barcelona, Spain

i_cantarero@ub.edu; galias@ub.edu; d.cruset@ub.edu; atrave@ub.edu

[b]Gas Natural Fenosa, Av. San Luís 77, 28033, Madrid, Spain, eloicarola@gmail.com

[c]Institute of Geological Sciences, University of Bern, Baltzestrasse 1+3, CH-3012 Bern, Switzerland, pierre.lanari@geo.unibe.ch

*Corresponding author: Irene Cantarero, i_cantarero@ub.edu.

Abstract

The relationships between deformation and fluid flow have been investigated in the Paleozoic basement of an isolated horst of the Catalan Coastal Ranges. A structural, petrological and geochemical study has been performed in a complex fracture network that resulted from a long-lived tectonic history (from Carboniferous to Miocene).

Nine fracture types, developed from a ductile regime in the greenschist facies to a shallow brittle regime, have been characterized in order to establish P, T and fluid compositions during the evolution of the horst. Syn-cleavage and late-cleavage quartz veins (qtz_1-chl_1±mu and late qtz_2-chl_2-dol_1) formed during the Hercynian ductile deformation. These minerals precipitated from metamorphic fluids, possibly evolved from seawater, at temperatures between 240 and 340ºC. En-echelon albite vein arrays (ab-qtz_3-chl_3±ti-an) and NE-SW normal faults generating breccias mark the change from ductile to brittle, from compression to extension and from a closed to an open hydrologic regime. This paragenesis precipitated from the mixing of metamorphic and magmatic fluids at temperatures

between 180 and 290ºC during the early Permian extension. Dolomite veins (dol_2-chl_4-qtz_4), precipitated at 210-280ºC from the mixing of previous fluids with hypersaline oxidizing external brines, possibly during the late stage of the early Permian extension. Reverse faults and calcite veins (Cc1-ba) formed either during the Paleogene compression or during the Langhian to early Serravallian minor compression. Calcite and barite precipitated from meteoric or marine waters in an open hydrological system at temperatures below 50ºC. The Miocene extension is represented by NE-SW normal faults with fault gouges and NNW-SSE normal faults cemented by calcite 2 that precipitated at temperatures below 50ºC from meteoric fluids in an open basin-scale hydrological system.

The studied horst was part of a relay zone between two segments of the NNW-SE Llobregat fault during the early Permian, explaining the high fracture density and the fast upflowing of hydrothermal fluids at that time, thus controlling the development of albite veins exclusively in this area.

***Key words**:* ductile deformation, brittle deformation, fluid flow, relay zone, crystalline Palaeozoic basement, Catalan Coastal Ranges.

1. Introduction

Fluids are ubiquitous in the Earth's crust and play a main role in diagenetic processes, metamorphism and the formation of ore deposits as they transport heat and dissolved ions (Fyfe et al., 1978; Ferry and Dipple, 1991; Deming, 1994; Garven, 1989; Duddy et al., 1994; Putnis, 2002; Trincal et al., 2015). A broad variety of fluid flow types occurs in the upper to middle crust, including flow along brittle faults and ductile shear zones, convection and pervasive fluid flow, which are driven by deformation and temperature gradients (Oliver, 1996, 2001). These fluid flow types cover a wide range of scales, from centimetric to regional scale (Oliver, 1996; Berwouts et al., 2008).

During shallow burial, fluids are produced by diagenetic reactions and by the expulsion of connate fluids during compaction, but external fluids may also enter in the system (Moore, 1989). As pressure

and/or temperature increase, and prograde metamorphic conditions are achieved, fluids are produced by devolatilization reactions of hydrous minerals contained in metasedimentary sequences (Walther and Orville, 1982; Ferry and Dipple, 1991; Connolly, 1997, 2010). Afterwards, during uplift, external fluids (basinal and meteoric) infiltrate in the rocks producing the retrogression of the rocks and the generation of new veins under different P-T conditions (Fyfe et al., 1978; Zhang et al., 2003; Anderson et al., 2004). Thus, during deformation and basin evolution, fluids evolve and change in terms of: 1) their hydrogeologic regime (open or closed) (Marquer and Burkhard, 1992; Travé et al., 1998; Ghisetti et al., 2001; Cruset et al., 2016); and, 2) their chemistry and composition due to e.g. fluid interaction with different lithologies, temperature and pressure changes that control the solubility/precipitation and stability barriers of minerals, redox reactions, fluid mixing caused by changes in the hydrogeologic regime and/or deformation, etc. (Barnaby and Rimstidt, 1989; Hanor, 1994; Labaume and Moretti, 2001; Parcerisa et al., 2006; Baqués et al., 2012; Lacroix et al., 2012).

On the other hand, fluid generation may increase the fluid pressure, which causes a decrease in the effective normal stress favoring failure and even induce the reactivation of misoriented faults at a given stress field (Sibson, 1977; Sibson and Scott, 1998; Aydin, 2000; Van Noten et al., 2011). Moreover, as fluids control the effective strength of rocks, they also exert a control in the transition zone between brittle and ductile conditions together with the geothermal gradient, lithology and grain size, inherited fabrics and stress field orientation (Connolly, 1997; Imber et al., 2001). Thus, fluids and deformation have an intrinsic relationship as fluids enable deformation and deformation facilitates fluid migration.

The study of veins, the best evidence of fluid flow, from a structural, petrological and geochemical point of view, provides insight about the relationship among deformation, metamorphism and fluid flow (Dewaele et al., 2004; Miller and Cartwright, 2006; Berwouts et al., 2008; Van Noten et al., 2008; Pitcairn et al., 2010; Depoorter et al., 2014). Quartz veins are present in most of exhumed metamorphic rocks and are generally believed to represent active fluid paths during or slightly after

deformation and metamorphism, thus registering the P-T path and fluid chemistry during and after metamorphism (Nesbitt and Muelenbachs, 1989; Wood and Walther, 1986; Yardley, 1986; Ferry and Dipple, 1991; Birtel and Stöckhert, 2008; Berwouts et al., 2008).

This work deals with the temporal and spatial relationship between fluids and deformation in an isolated horst of the Catalan Coastal Ranges (NE Iberia), mainly constituted of Ordovician phyllites. This horst, the Turó de les Forques, is differentiated from the surrounding areas by a complex network of fractures including syn- to late-cleavage Hercynian veins and faults and veins generated during different extensional and compressional events registered in the Catalan Coastal Ranges. The relationships between deformation and fluid flow in the Mesozoic and Cenozoic tectonic events have been previously studied in Mesozoic and Neogene carbonates (Travé et al., 1998; Baqués et al., 2010, 2012) and also in Neogene siliciclastic rocks (Travé and Calvet, 2001; Travé et al., 2009; Parcerisa et al., 2005; Cantarero et al., 2014a). For the first time, in this work, the study of such relationships is focused in the metamorphic Paleozoic basement in order to decipher the behavior of a crystalline basement with respect to fluids from Hercynian to Neogene times.

The aims of this study are fourfold: (i) to characterize petrologically and geochemically the mineral paragenesis related to the different generations of fractures; (ii) to determine the composition and origin of fluids; (iii) to establish the hydrogeological regimes and the fluid pathways as a function of the involved tectonic event; and (iv) to decipher the structural evolution of this isolated horst and why it concentrates that high density of fractures.

2. Geological Setting

The Catalan Coastal Ranges (CCR), located in NE Spain, are the result of a long tectonic history that spans from Paleozoic to Present times. Nowadays, the CCR display a well-developed NE-SW horst-and-graben structure acquired during the opening of the Valencia Trough (Oligocene-early Miocene) (Roca and Guimerà, 1992). This structure is limited by NE-SW striking listric normal faults (fig. 1),

with a detachment level at 12-16 km (Gaspar-Escribano et al., 2004), segmented by later NW-SE to NNW-SSE trending faults. This Neogene extensional structure is superimposed on a Paleogene contractional structure, the Catalan Intraplate Chain, formed during the N-S collision between the Iberian and European plates during Late Cretaceous-late Oligocene (Guimerà, 1984; Bartrina et al., 1992). In its turn, NE-SW Paleogene thrusts were the result of the inversion of major Mesozoic normal faults (Guimerà, 1984; Bartrina et al., 1992; Roca, 1994; Vergés and García-Senz, 2001) that resulted from the western Tethys and of the North Atlantic openings. Moreover, previously to these tectonic events, Hercynian deformation and late-Hercynian processes also took place as recorded by the outcropping Paleozoic rocks within the horsts (Julivert and Durán, 1990a, b; Santanach et al., 2011; Cantarero et al., 2012, 2014b). In general, three Hercynian deformation phases have been reported: a main deformation phase responsible of the E-W trending folds and a main regional foliation and two late folding phases that formed crenulations to chevron and kink folds and related cleavages (Julivert and Durán, 1990a). After these folding phases, but before Triassic, late-Hercynian acidic to intermediate plutonic and hypabyssal rocks intruded the Cambro-Ordovician to Lower Carboniferous metamorphic sequence (Enrique, 1990). On a larger scale, this orogeny generated the curved Ibero-Armorican belt caused by the oblique convergence and collision of Gondwana and Laurentia-Baltica supercontinents at the end of the Paleozoic (Matte, 2001). The CCR belong to the northern limb of this arc where mainly greenschist facies conditions were acquired (Julivert and Duran, 1990b).

The Turó de les Forques is a horst, constituted by Ordovician phyllites, isolated within the Miocene rocks of the Vallès Half-graben, which is separated to the west from the Garraf Massif by the incision of the Llobregat River (fig. 1). These rocks are unconformably overlain to the north by Miocene rocks, gently dipping to the NW, and are limited to the E by NNW-SSE and NE-SW striking normal faults dipping to the E-SE. At the other side of the Llobregat river, Ordovician phyllites are unconformably overlain by Buntsandstein facies (fig. 1). Both Buntsandstein and Miocene

126 successions are only gently tilted (10-20º), indicating the scarce rotation of the rocks forming the
127 Turó de les Forques.
128 The incision of the Llobregat River has exposed a 500 m long and 80 m high excellent outcrop,
129 intensely crosscut by a huge amount of fractures resulting from a complex tectonic history from
130 Hercynian to Neogene times.
131
132 **3. Methodology**
133 The field work carried out in this study allowed to generate a schematic map and a cross-section of
134 the Turó de les Forques (fig. 2). Structural data was collected and plotted in equal-area lower-
135 hemisphere stereographic projections (fig. 3). The remarkable outcrop parallel to the highway was
136 mapped and the different fractures sets and their crosscutting relationships were established (fig. 3).
137 The different generations of fractures, fault rocks and vein minerals, were sampled. Thin sections
138 were studied under optical and cathodoluminescence microscopes. A Technosyn Cold
139 Cathodoluminescence Model 8200 MkII operating at 16-19 kV and 350 µA gun current was used.
140 X-ray diffractions of 7 whole-rock powders have been performed with a Bragg-Brentano PAnalytical
141 X'Pert PRO MPD alpha 1 operating at 1.5406 Å, 45 kV and 40 mA. They were scanned from 4 to
142 100º2θ with a 0.017º2θ step size and a count time of 50s per step. Oriented aggregates of clay minerals
143 in gouges were also prepared in order to recognize the mineralogy. Samples were dispersed and
144 disaggregated by soaking in de-ionized water and suspended repeatedly. Separation of the <2 µm
145 fraction was done by centrifugation. Samples were subsequently air-dried, glycolated during 24 hours
146 at 50ºC and heated for 2h at 550ºC. XRD patterns were obtained between 2 to 62º2θ (normal sample)
147 and 2 to 30º2θ (ethylene glycol and thermal treatment samples) with a 0.033º2θ step size and a count
148 time of 50 s per step.
149 Ordovician phyllites and gouges have also been analyzed by X-Ray Fluorescence (FRX). Major
150 elements were measured in fussed samples with a Panalytical PW 2400 spectrophotometer, using an

Rh anode. Fussed samples were prepared with 0.3 g of molten and dry sample mixed with 5.7 g of lithium tetraborate and 5 mg of lithium iodide. The mixture was homogenized and fussed at 1125ºC obtaining pearls of 30 mm of diameter.

Carbon-coated thin sections were used to analyse major and minor elements of carbonate cements, chlorites, feldspars and micas with a CAMECA SX-50 electron probe micro-analyzer (EPMA). It was operated using 15 nA beam intensity, 20 keV acceleration voltage and a beam diameter of 10 μm. The precision of major elements is about 0.64% (at 2σ confidence level).

Twelve microsamples of calcite cements were powdered with a microdrill for carbon and oxygen isotopes. Samples (60±10μg) were reacted with 100% phosphoric acid at 70º C for three minutes. The CO_2 extraction was done in an automated Kiel Carbonate Device III attached to a Thermal Ionization Mass Spectrometer Thermo Electron (Finnigan) MAT-252 following the method of McCrea (1950). The International Standard NBS-19 was used. The results are expressed in ‰ VPDB standard. Standard deviation is ±0.02‰ for $\delta^{13}C$ and ±0.07‰ for $\delta^{18}O$.

Temperature conditions were estimated both, by thermometry from chlorite composition and by fluid inclusion analyses.

Chlorite present several chemical substitutions (simple and coupled) controlled by the equilibrium conditions (P, T, pH, fO_2) that can be modeled using a set of different end-members (Vidal et al., 2001, 2005, 2006, 2016; Lanari et al., 2014). In this work the multi-equilibrium approach of Vidal et al. (2005, 2006) was used to obtain the simultaneous estimate of Fe^{3+} content in chlorite and equilibrium temperature by the convergence of four equilibria reactions involving five chlorite end-members (Mg-amesite ($Si_2Al_4Mg_4O_{10}(OH)_8$), Fe-amesite ($Si_2Al_4Fe_4O_{10}(OH)_8$), daphnite ($Si_3Al_2Fe_5O_{10}(OH)_8$), clinochlore ($Si_3Al_2Mg_5O_{10}(OH)_8$), and sudoite ($Si_3Al_4Mg_{2\square 1}O_{10}(OH)_8$)) at a given pressure (Vidal et al., 2005). The position of these equilibria in a P-T space depends on the activities of the chlorite end-members, quartz and water (Berman, 1991). In this work, temperatures and XFe^{3+} of chlorite were estimated at a fixed pressure of 2 kbar, taking into account that Hercynian

metamorphism is LP-HT and that a pressure of 1.5 kbar has been reported for the late-Hercynian granodiorite intruding the Ordovician host rocks in a nearby area at the Littoral Chain (Gil-Ibarguchi and Julivert, 1988). Water activity has been considered equal to 1. The convergence is achieved for a minimum Fe^{3+} fraction ($XFe^{3+} = Fe^{3+}/(Fe^{2+}+Fe^{3+})$ when the temperature difference between the four equilibria is less than 30ºC (Lanari et al., 2012 and references therein). Formation temperatures of chlorite in the current study were estimated using the program CHLMICAEQUI (Lanari, 2012).

Fluid inclusions were examined in quartz and calcite to determine composition and temperature of the mineral-forming fluid. Thick sections were used for petrographic characterization of the fluid inclusions and for microthermometric determination. Measurements were made on a Linkam THM-600 heating-freezing stage. Raman microspectroscopy analyses were recorded with a LabRam HR800 Jobin-Yvon^{TM} microspectrometer equipped with 600 g/mm gratings and using 532 nm (green) laser excitations. Acquisition timespan was 30 s and 60 s during 10 accumulation spectra. Vapor bubbles were analyzed in order to determine the presence of volatile species (CO_2, CH_4, N_2, H_2S). Due to fluorescence interferences, fluid inclusions only have been analyzed in quartz 1.

4. Structure

The Ordovician phyllites show a regional foliation that dips dominantly 60º to the NNE which is deformed by km-spaced WNW-ESE open folds (fig. 2, 3). The foliation corresponds to a penetrative cleavage which is locally deformed in centimetric kink folds with axial planes dipping around 80ºE. These orientations are consistent with the Hercynian structures described at regional scale (Julivert & Duran, 1990a). The phyllites are intruded by two granodioritic porphyries of NE-SW direction.

Based on field and thin section cross-cutting relationships, orientation, geometry and vein mineralogy, 9 fracture types have been described, being from the oldest to youngest: syn-cleavage quartz veins, late-cleavage quartz veins, en-echelon albite veins, NE-SW normal faults, NE-SW dolomite veins, NW-SE reverse faults, N-S calcite veins, NE-SW Neogene normal faults and NNW-

SSE Neogene normal faults. The first seven generations have only been found in the Ordovician phyllites whereas the last two fault systems affect both Ordovician phyllites and Miocene rocks.

Syn-cleavage quartz veins. Veins are from 1 to 50 cm wide and are concentrated into 4-meter thick bands separated by a metric spacing. Veins occur in moderate to tight rounded folds with axial-planes parallel to cleavage. In the limbs the veins are dismembered parallel to the cleavage, whereas in the hinge, veins are thickened (fig. 3, 4A). These observations point out that these veins are coeval to the development of the Hercynian cleavage.

Late-cleavage quartz veins. These veins cross-cut the previous quartz veins and are less abundant. They are 1 to 7 cm wide and up to 1 m long and are developed perpendicular to the cleavage (fig. 3, 4B). However, locally, they are slightly deformed by open folds, which axial plane is the regional cleavage. That relationship suggests that these veins were formed during the last stages of the cleavage development. Moreover, at microscopic scale, these veins are affected by discontinuous ductile shears, about 2 cm long and 200-500 µm wide, subparallel to the vein walls, thus confirming the Hercynian age of these veins.

En-echelon albite veins. Veins have a N-S to NE-SW striking direction with a steep dip towards the W (fig. 3). Veins are from 3 to 15 cm long and from 1.5 mm to 5 cm wide and have both straight and sigmoidal shapes (fig. 4C, D). They have a characteristic pinkish color due to the albite. The thickest veins usually contain angular phyllite clasts (fig. 4E). Also the coalescence of several veins produced a brecciation of the rock. These veins are not homogeneously distributed along the outcrop. They are disseminated in the host rock with densities from 11 to 75 fractures/m or are arranged in en-echelon vein arrays (fig. 3, 4). Such arrays are both single and conjugate sets with a mirrored symmetry and indicate a normal displacement. In some cases, these arrays are linked to discrete fault planes (fig. 4D).

NE-SW normal faults. Faults are normal and transtensional with a dominant NE-SW trend and dips between 63 and 87º indistinctly to the NW or SE, in a conjugate system. Plains are usually undulouse,

producing variations in the strike direction (fig. 3). These faults generate breccias constituted by angular clasts derived from the phyllites, up to 3 cm in size, and from albite veins, which are in turn cemented by albite. This fact suggests successive fault movements and albite precipitation. Locally these faults have been reactivated as strike-slip. This reactivation generates greenish cohesive cataclasites constituted by millimetric to centimetric clasts from the host rock and albite veins (fig. 4F).

NE-SW dolomite veins. These veins, up to 400 µm wide and up to 3 cm long, have only been recognized at microscopic scale. They show a NE-SW trend with dips between 35-45ºSE.

NW-SE reverse faults. This set of fractures are poorly developed and represents reverse faults defined by NW-SE discrete planes dipping around 35º to the NE (fig. 3).

N-S calcite veins. These veins, up to 2 mm wide, have been only recognized at microscopic scale. They show a N-S striking direction and are subhorizontal.

NE-SW Neogene normal faults. This system affects both the Ordovician phyllites and the Miocene rocks, thus indicating their Neogene age. They are represented by NE-SW normal faults with dips from 25 to 80 mostly to the NW (fig. 3). This dip variability is caused by the characteristic fan-like geometries of this system (fig. 3). These geometries are formed by both discrete planes or up to 1.5 m wide fault cores, only in the phyllites, defined by greyish fault gouges (fig. 4G).

NNW-SSE Neogene normal faults. These faults cut and displace the Miocene unconformity and the Miocene rocks above, indicating their formation during the Neogene extension (fig. 3B).This fault system is defined by a conjugate system of NNW-SSE trending normal faults dipping 52-79º indistinctly to the W or E, later reactivated as strike-slip faults (fig. 3B-C). These faults are represented by discrete planes that locally develop centimetric fan-like geometries. This system commonly has striated planes, which are sometimes formed by calcite slickenlines (fig. 3B).

5. The host rocks

Phyllites are characterized by a penetrative cleavage defined by a strong preferred orientation of chlorite, muscovite and elongated quartz with some interbedded quartz-rich layers, from 0.1 to 1.8 mm thick (fig. 5A-C). Bedding shows syn-cleavage tight folds with thickened hinges, with axial planes and limbs parallel to the regional foliation (fig. 5B). This foliation is locally folded by minor crenulations (fig. 5D) and kink folds.

Pelitic bands are constituted by muscovite (60%), quartz (25%), chlorite (10%) and albite (5%) and are rich in organic matter. Muscovite crystals range in size from 0.01 to 0.05 mm, quartz and albite from 0.02 to 0.1 mm and chlorite from 0.05 to 0.15 mm. On the other hand, quartz-rich layers have a granoblastic texture constituted by quartz (60%), muscovite (35%) and chlorite (5%). Quartz has a grain size between 0.05 and 0.1 mm, muscovite between 0.02 and 0.15 mm and chlorite between 0.1 and 0.2 mm. Quartz and chlorite are elongated parallel to the regional foliation and show intracrystalline deformation, indicating a pre-foliation development (fig. 5A, C), whereas the preferred orientation of prismatic muscovite crystals (fig. 5C), points to a syntectonic crystallization.

Miocene rocks from the Costablanca Formation (Burdigalian; Anadón and Cabrera, 1980; Cabrera, 1981), unconformably overlying the Ordovician phyllites, consist of an alternance of lacustrine carbonates, red conglomerates and white to red lutitic layers. Lacustrine carbonates are mudstones with levels rich in filamentous microbial-like structures and a dull orange cathodoluminescence.

Miocene limestones show $\delta^{18}O$ values between -8.6 and -8 ‰VPDB and $\delta^{13}C$ values between -7.7 and -6.5 ‰VPDB (fig. 6).

6. Paragenetic sequence in fractures

The 9 different fracture types described above are characterized by different mineral associations, leading to the following paragenetic sequence (fig. 7):

6.1. Quartz 1-chlorite 1±muscovite

This mineral association constitutes the main paragenesis of the syn-cleavage and late-cleavage quartz veins. In both types of veins, quartz 1 crystals are inequigranular, up to 7 mm in size, inclusion-rich and have undulouse extinction (fig. 8A). Quartz crystals in syn-cleavage veins show intracrystalline deformation and partial recrystallization represented by subgrain formation, deformation lamellae and lobate grain boundaries (fig. 8A). This intracrystalline deformation is less intense in late-cleavage quartz veins, which crystals are elongated and bladed and grain boundaries are straight or curved.

Chlorite 1 grows along the contact between quartz crystals. It is characterized by brownish crystals up to 62 µm in size. Though less abundant, muscovite flakes up to 200 µm are associated with chlorite (fig. 8B). Chlorite and muscovite of the host rock form larger crystals, up to 350 µm, along the contact with the quartz-vein probably due to host rock recrystallization during vein formation (fig. 8C).

6.2. Quartz 2-chlorite 2-dolomite 1

This mineral association is related to discontinuous ductile microshears and microveins developed in the late-cleavage quartz veins (fig. 8D-E). This late stretching also caused the elongation of quartz crystals, perpendicularly to the veins, with this mineral association precipitating in the triple points between the elongated quartz crystals (fig. 8F).

Quartz 2 crystals have less inclusions than the previous quartz generation and grow in optical continuity with the hosting quartz 1 crystals. Dolomite 1 cement is characterized by rhombic and subhedral crystals, 60 µm and 50 to 100 µm in size, respectively. Chlorite 2 is characterized by vermicular morphologies, from 53 to 174 µm long and from 15 to 50 µm wide, and it is included within the quartz 2 crystals and dolomite 1 crystals (fig. 8E-F).

6.3. Albite-quartz 3-chlorite 3±titanite-anatase

This paragenesis is found in en-echelon albite veins and breccias formed in the NE-SW normal faults.. A temporal evolution is observed in these veins:

The first veins, up to 1.5 mm wide, are characterized by the presence of elongated to euhedral albite and quartz (fig. 9A). These incipient veins are crosscut by straight and sigmoidal veins mainly formed by albite. These types of veins postdate the minor crenulations formed during the late Hercynian folding phases (fig. 9B). During and after late veining, breccias were also formed (fig. 9C). In this deformation, albite is characterized by prismatic crystals, from 50 to 770 μm in size, with Carlsbad twinning. The albite has a composition above 95% albite, as shown by EPMA, and it is usually altered to kaolinite. Quartz 3 is inclusion-free, and forms 150-400 μm in size subhedral crystals. Chlorite 3 is characterized by 30-60 μm in size vermicular crystals included in the albite and quartz crystals and fibrous-radial aggregates, with 300 μm long fibers, between crystals and forming planes at vein walls (fig. 9D-E). Titanite and anatase grains are occasionally found (fig. 9F).

6.4. Dolomite 2-chlorite 4-quartz 4

This paragenesis is developed in the NE-SW dolomite veins and vugs affecting the quartz 1 crystals (fig. 10) and postdates the albite-quartz3-chlorite3±titanite-anatase association (fig. 10A). Vugs are up to 1 mm in diameter and have irregular borders (fig. 10E-F). Quartz 4 is inclusion-free and grows in optical continuity with the hosting quartz crystals. Dolomite 2 is represented by dull red, 50 to 340 μm, subhedral crystals in fractures and 100 μm in size rhombs with a dull red to orange concentric zonation in vugs (fig. 10B-F). Finally, chlorite 4 has vermicular morphologies associated to dolomite fractures and forms irregular masses in vugs (fig. 10B-C, E).

Dolomite is characterized by $\delta^{18}O$ values between -6.3 and -5.4 ‰VPDB and $\delta^{13}C$ values between -11.7 and -11.4 ‰VPDB (fig. 6).

6.5. Calcite 1-barite

This association is present in the N-S subhorizontal calcite veins and partially cementing the cataclasites produced during the strike-slip reactivation of NE-SW normal faults.

Calcite 1 is characterized by euhedral drusy, 40 μm to 1 mm in size, crystals with a zoned orange cathodoluminescence (fig. 10D, 11A-B). Barite forms prismatic crystals, up to 1.5 mm long and 140 μm wide and, together with calcite 1, cements the cataclasites and microfractures in quartz 1 crystals (fig. 11C-D).

The calcite 1 shows $\delta^{18}O$ values between -9 and -6.5 ‰VPDB and $\delta^{13}C$ values between -12.7 and -9.7 ‰VPDB (fig. 6).

6.6. Gouges

Greyish fault gouges are formed in the NE-SW Neogene normal faults. They are constituted by quartz, muscovite, chlorite, albite and anatase resulting from the comminution of the phyllites and newly formed illite, smectite and kaolinite. Fault gouges change moderately the global bulk composition of the Ordovician phyllites, represented by a decrease of the SiO_2 content together with an increase in Al_2O_3 and K_2O. This is consistent with an increase of white mica (illite formation) and loss of chlorite in the gouges respect to the host rock.

6.7. Calcite 2

Calcite 2 cement is present in the NNW-SSE Neogene fractures. It is characterized by subhedral crystals, from 80 to 520 μm in size, with orange luminescence and a drusy disposition in the main fault planes (fig. 12A-B) and by subhedral to rounded crystals, from 60 μm to 1 mm in size, with orange to non-luminescent zonation and a blocky disposition in joints (fig. 12C-D).

Calcite 2 cement has $\delta^{18}O$ values between -15 and -12.2 ‰VPDB and $\delta^{13}C$ values between -7.4 and -6.3 ‰VPDB (fig. 6).

7. Thermometry

7.1. Chlorite chemistry and T- XFe^{3+} estimates

The chemical composition of chlorites in the phyllites (abbreviation: chl_0) and the four vein-filling paragenesis (chlorites 1 to 4, abbreviations: chl_1, chl_2, chl_3, chl_4) was determined by EPMA. Two main groups are distinguished based on variations in SiO_2, FeO, MgO and MnO contents. The first group is formed by the chlorite in the host rocks chl_0 and chlorites chl_1, chl_2 and chl_3. SiO_2 ranges between 24 and 28.6 wt.%, FeO between 20 and 36.8 wt.% (with mean values slightly lower in the phyllites), MgO between 4.9 and 19.6 wt.% and MnO between 0.1 and 1 wt.%. On the other hand, the second group formed by chl_4 exhibits higher SiO_2, MgO and MnO contents (26.7-29.6 wt.%, 13.4-19.3 wt.% and 0.3-2.9 wt.% respectively), and slightly lower FeO content (19.4-28.3 wt.%). Similar trends are observed in the structural formula composition expressed in atom per formula unit (apfu). Si content ranges between 2.6 and 2.8, Fe between 2.2 and 3.4, Mg between 0.8 and 2.3 and Mn between 0.015 and 0.1 in the chl_{0-3} and, between 2.8-3 apfu, 1.6-2.5, 2.1-2.9 and 0.02-0.26, respectively, in chl_4 (fig. 13). Thus, according to Foster (1962), chl_{0-3} are dominantly classified as ripidolites and chl_4 as brunsvigites. However, Al_2O_3 ranges between 22.9 and 23.2 wt.% in Chl_0, 19-24.2 wt.% in chl_{1-3}, and 16.7-21.9 wt.% in chl_4. Major differences are produced in the Al^{VI} position with: 1.5-1.7 (chl_0), 1.2-1.6 (chl_{1-3}) and 1.1-1.4 (chl_4) whereas Al^{IV} is 1.1-1.4 (chl_{0-3}) and 1-1.2 (chl_4). Crystallization temperature and XFe^{3+} of chlorite were estimated using the calibration of Vidal et al. (2005, 2006). Convergence was not achieved in the P-T-XFe^{3+} space for the chl_0 composition observed in the phyllites. Chl_1, chl_2 and chl_3 are characterized by low XFe^{3+} values of 0.07-0.33 (0.14 in average) and temperatures ranging between 237 and 343ºC (290ºC in average) (fig. 13). By contrast, chl_4 are characterized by higher XFe^{3+} of 0.46 ± 0.06 and slightly lower temperatures, ranging between 234 and 309ºC (261ºC in average) (fig. 13).

7.2. Fluid inclusions

375 Fluid inclusions analyses have been performed in quartz and calcite veins.

376 The petrographic analysis revealed that quartz 1 (qtz_1-chl_1-mu), quartz 3 (qtz_3-ab-chl_3) and quartz 4
377 (qtz_4-chl_4-dol_2) are characterized by small (2-10 µm) primary aqueous biphase liquid-rich fluid
378 inclusions (25% vol. gas bubble), suitable for microthermometry measurements. On the other hand,
379 in calcite 1 and 2, primary monophase aqueous fluid inclusions, between 2 and 12 µm in size,
380 observed in growth zones of calcite crystals remained monophasic after cooling for 7 days at 4°C.

381 Fluid inclusions in quartz 1 show homogenization temperatures between 230 and 370ºC (with most
382 values between 240 and 320ºC), quartz 3 between 140 and 310ºC (180-270ºC) and quartz 4 between
383 157 and 330ºC (180-300ºC) (fig. 14). Thus, the four quartz generations show very similar range of
384 temperatures, with a slight temperature decrease in quartz 3 and 4. The pattern and the absolute values
385 are both in line with the results obtained by chlorite thermometry.

386 In all the quartz generations, melting temperatures above 0ºC were obtained, indicating the presence
387 of clathrates. Salinities, for the negative T_m values, were calculated in the binary H_2O–NaCl system,
388 using the equation of Bodnar (1993). In quartz 1, T_m ranges between -6 and +8ºC (fig. 14), obtaining
389 salinity values between 0 and 7 wt% NaCl eq.. Quartz 3 T_m ranges between -9 and +3 ºC, indicating
390 salinities between 7.8 and 12.8 wt% NaCl eq.. Finally, quartz 4 has the highest T_m variability, between
391 -21 and +9ºC (fig. 14), indicating salinities between 0 and 23 wt% NaCl eq.. The highest salinities,
392 20-23wt% NaCl eq., are related to the lowest T_h ranging between 157-232ºC.

393 Raman analyses in fluid inclusions of quartz 1 showed the presence of 0-3% CH_4 and 0-41% N_2 in
394 addition to 57-100% CO_2.

395

396 **8. Discussion**

397 **8.1. Evolution from ductile to brittle deformation and related fluid**

398 The association quartz-chlorite-muscovite-albite of the Ordovician phyllites of the Turó de les
399 Forques indicate their formation during greenschist facies. The absence of biotite suggests that they

400 formed at temperatures *ca*. 400ºC. The absence of intersection between the chlorite-quartz-water
401 equilibria in the P-T-XFe^{3+} space for chl_0 could suggest formation temperature higher than 380ºC at
402 low pressure (Lanari, 2012).
403 Syn-cleavage and late-cleavage quartz veins are highly frequent in Paleozoic low-grade metamorphic
404 rocks along the CCR, as occurs in most metamorphic rocks, as they are inherently related to
405 deformation and Si-rich fluids derived from metamorphism (Birtel and Stöckhert, 2008). The
406 presence of carbonate in the metapelites, as pointed by Gil-Ibarguchi and Julivert (1988), could be
407 the source for dolomite 1. Also, the presence of the CO_2-N_2-CH_4 mixture in fluid inclusions is
408 compatible with metamorphic fluids produced by devolatilization reactions and fluid-rock interaction
409 in sedimentary sequences rich in organic matter under low-grade metamorphic conditions (Shepherd
410 et al., 1991; Dee and Roberts, 1993; Yardley, 1997; van der Kerkhof and Thiéry, 2001; Kenis et al.,
411 2005). Their related mineral paragenesis, chl_1-qtz_1-mu and chl_2-qtz_2-dol_1, show slightly lower
412 temperature conditions than the host rock, 240-340ºC, as suggested by both fluid inclusions and
413 chlorite thermometry. This result suggests that the veins formed at slightly lower temperatures than
414 the ones achieved during the metamorphic peak.
415 It has been suggested that metamorphic fluids are the result of the continuous evolution of
416 sedimentary pore fluids that are modified during diagenesis and metamorphism by devolatilization
417 reactions as fluids interact with the host rocks at different P-T conditions (Yardley, 1997; Yardley
418 and Graham, 2002). The protolith of the Ordovician phyllites consist of greywackes and shales
419 deposited in deep-sea turbiditic sequences of a passive margin (Vilà and Pin, 2016). Salinities
420 obtained from fluid inclusions in quartz 1 are similar to those of seawater (3.5 wt% NaCl eq.),
421 suggesting that the metamorphic fluid has evolved from a marine connate fluid. Small salinity
422 variations from this value can result from the addition of Cl due to Cl-OH and Cl-F exchange reactions
423 between the fluid and hydrous minerals (salinity increase) and dehydration reactions produced during

424 burial and prograde metamorphism (salinity decrease) (Smith and Yardley, 1999a,b; Yardley and
425 Graham, 2002; Vidal and Dubacq, 2010).
426 At mesoscale, quartz veins evidence fluid flow along fractures. Dehydration metamorphic reactions
427 supply large volumes of silica-rich fluids during cleavage development that favours the formation of
428 syn-cleavage veins formation. During the last stages of cleavage development, the remaining volume
429 of silica-rich fluids is lower as observed with the minor development of late-cleavage veins. We
430 interpret that this late cleavage-perpendicular fracturing was triggered by the decrease in overburden
431 pressure caused by the denudation of the orogen, which produced a relative fluid pressure increase in
432 a ductile regime. On the other hand at microscale, fluid flow also occurred along microshears and
433 intercrystalline boundaries and precipitated in low-pressure areas such as triple points created
434 between elongated quartz crystals (fig. 15). Such a fluid flow, through interconnected grain
435 boundaries and triple points, was favored by the temperature conditions. Below 300ºC and low
436 pressures, the cooling contraction of quartz together with its extremely low diffusion and the stop of
437 grain boundary migration generated the opening of grain boundaries (Kruhl et al., 2013). Thus, during
438 metamorphism a coupled fluid flow system acted: a regional channelized fluid flow system giving
439 rise to the mesoscopic quartz veins and a centimetric scale pervasive flow through grain boundaries
440 and triple points.
441 After the development of quartz veins, the formation of albite veins and albite-cemented breccias in
442 the NE-SW normal faults suggests a progressive change in the fluid composition indicated by the
443 change from quartz-enriched to albite-dominated paragenesis. As no ductile deformation structures
444 neither recrystallization textures have been observed related to albite veins, a brittle regime is
445 interpreted in the formation of these veins. Therefore, the compositional variation of the fluids, from
446 silica-rich to albite-rich, occurred during the transition from ductile to brittle conditions (fig. 16).
447 Moreover, the shear sense of the en-echelon vein arrays and the NE-SW normal faults indicate their
448 formation during an extensional stress regime. At regional scale, two different deformation phases

could cause the extensional structures: the early Permian extension and the late Permian-Early Jurassic rifting. The former, resulting from the collapse of the Hercynian orogen and associated with magmatism and the development of grabens filled with Permian deposits, has been observed in the Pyrenees and other European regions (i.e. Central French Massif, Alps, German Basin, Ardenne Belt, Sardinia, Arthaud and Matte, 1977; Ziegler, 1988; Faure, 1995; Deroin, 2003; Lago et al., 2004; Depoorter et al., 2014), but not in the CCR, up to now. On the other hand, the latter, although being recognized in the area (Salas et al., 2001), supposes a long-time gap since the end of the Hercynian orogeny (Carboniferous) to let the gradual fluid composition change between the compressional and extensional structures. Moreover, during this time interval, at the end of the Permian, there is a tectonic quiescence stage, registered by the peneplain weathering surface identified in Europe on Paleozoic rocks before the Buntsandstein facies deposition (Gómez-Gras and Ferrer, 1999; Parcerisa et al., 2010). Nevertheless, despite the absence of Permian sedimentation and volcanism in the CCR, Marzo (1979) proposed that the basins delimited by NW-SE faults, where sedimentation of the Buntsandstein facies occurred, were probably formed during the early Permian extension as these facies fossilize the faults. Besides, it is important to highlight that these facies, which unconformably overlay the Ordovician phyllites at the other side of the Llobregat fault (fig. 1), are not affected by these en-echelon albite veins, thus marking their previous formation. Therefore, we consider that the en-echelon veins and faults cemented by albite are a direct evidence that this early Permian extension also took place in the CCR. Temperature estimates by chlorite thermometry and fluid inclusions indicate a similar range of temperatures than the previous paragenesis, 180-290ºC. However, significant exhumation had already occurred during and after the Hercynian deformation, as synorogenic Carboniferous sandstones (Culm facies) contain clasts made of Ordovician to Tournaisian rocks (Martínez et al., 2016). In fact, as said before, the basal Buntsandstein conglomerates unconformably overlay the Ordovician phyllites, indicating exhumation of the Ordovician rocks during the Permian. Thus, such exhumation implies that the albite paragenesis

474 precipitated from hydrothermal fluids and/or that the geothermal gradient increased highly above
475 40ºC/km (minimum gradient acquired during metamorphism in the area). Such fluids had higher
476 salinities than the previous ones, from 7.8 to 12.8 wt% NaCl eq., and were Na-rich in order to
477 precipitate albite and Ti-rich in order to precipitate titanite and anatase. Calc-alkaline porphyries
478 intruded the phyllites after Hercynian folding stages but previous to Triassic times (Enrique, 1990).
479 The fluids related to these intrusions were hot and Na-rich, as denoted by the porphyry composition,
480 and also could carry titanium. Moreover, salinities up to 10 wt% NaCl eq. have been observed in
481 veins of epithermal and porphyry deposits related to calc-alkaline magmatism (Heinrich, 2005).
482 Therefore, the progressive entrance of magmatic fluids related to these late-Hercynian granodioritic
483 porphyries may have mixed with the previous metamorphic fluids, explaining the composition,
484 temperature and salinity of these hydrothermal fluids. Also the stop of the prograding metamorphism
485 could explain the salinity increase through the end of dehydration reactions that lowered the salinity
486 by water release (Kenis et al. 2005; Berwouts et al., 2008).
487 The following dolomite 2-chlorite 4-quartz 4 veins mark a change in the physico-chemical
488 characteristics of the fluid, as the increase in XFe^{3+} in Chl_4 indicates a more oxidizing character of
489 the fluid (fig. 13) (Lanari et al., 2014; Trincal et al., 2015). Two scenarios can be invoked to produce
490 such a shift in the oxidation conditions: (1) a temperature drop and/or (2) a chemical variation of the
491 rock (Mickucki and Ridley, 1993; Dewaele et al., 2004). Chlorite temperature estimates and fluid
492 inclusions analyses indicate slightly lower precipitation temperatures, between 210 and 280ºC.
493 However, for a fixed bulk rock composition and a temperature decrease of 50ºC, XFe^{3+} only rises
494 0.06-0.08 (see trends in fig. 13), being here the shift much higher (0.15-0.35). Thus, an external
495 perturbation is required to significantly affect the redox conditions. Fluid inclusions reveal a fluid
496 mixing line between hot, low to intermediate salinity fluids (recycled from the previous paragenesis)
497 and a subordinate low temperature (140-200ºC) high salinity fluid (fig. 14). Thus, the change in the
498 oxygen fugacity is probably due to the entrance of a colder and very oxidizing external brine.

Applying the equation of Fritz and Smith (1970) for dolomite 2, with $\delta^{18}O$ values between -6.3 and -5.4 ‰VPDB and T between 140 and 280ºC, the $\delta^{18}O$ of the fluids ranges between +7.4 and +19.8 ‰VSMOW. These values confirm that fluids derived or are in equilibrium with metamorphic and igneous rocks and were mixed with a more $\delta^{18}O$-depleted brine (Taylor, 1967, 1977). In turn, the highly ^{13}C-depleted values of dolomite 2 indicates that there was no expulsion of aqueous fluids with CO_2 derived from carbonate rocks from the Paleozoic sequence, which are represented by Ordovician carbonates interbedded with the phyllites and Devonian carbonate rocks (Rumble et al., 1986). On the contrary, these values may record, on one hand, the production of $\delta^{13}C$-depleted CH_4 during metamorphism and, on the other hand, the production of $\delta^{13}C$-depleted CO_2 during this oxidizing stage, through the oxidation of the carbonaceous material contained in the metapelites and/or the oxidation of $\delta^{13}C$-depleted CH_4 produced during metamorphism (Taylor and O'Neil, 1977; Rumble et al., 1986). This CO_2 content increase probably caused a change in the XCO_2 gradient, favoring the stability of carbonates in this stage (Mickucki and Ridley, 1993). This increase in CO_2 lowers the water activity and thus may affect the chlorite and XFe^{3+} estimates made with the model of Vidal et al. (2005, 2006). For chl_4, the model predicts equilibrium at 264 ± 18°C for a XFe^{3+} of 0.46 ± 0.08 assuming $aH_2O = 1$, 240 ± 19 °C for a XFe^{3+} of 0.47 ± 0.07 assuming $aH_2O = 0.4$ and 222 ± 17 °C for a XFe^{3+} of 0.48 ± 0.07 assuming $aH_2O = 0.2$ (details in supplementary material S1). This comparison shows that the temperature slightly decreases with decreasing aH_2O, whereas XFe^{3+} is not affected by aH_2O. The predicted decrease of T is however small and remain close to the analytical uncertainty and the model returns values that are in line with the T recorded by the fluid inclusions. Taking into account these observations, dolomite veins were probably formed during the last stages of the early Permian extension during ongoing exhumation (fig. 16).

Reverse and strike-slip faults observed at mesoscale have been related to the N-S subhorizontal calcite veins according to the similar structural orientation. All these structures, which are a minor phase in the Turó de les Forques, have been related to a compressional event. Vein minerals in this stage are

524 different from previous deformational phases revealing a major change in the fluid composition and
525 origin. Calcite 1 and barite are present instead of chlorite and quartz and, as indicated by the presence
526 of monophasic fluid inclusions (Goldstein and Reynolds, 1994), this mineral paragenesis precipitated
527 at low temperatures, below 50ºC. The presence of barite indicates that the low-temperature fluid
528 contained dissolved SO_4^{2-}, suggesting the presence of seawater or of meteoric water that has
529 remobilized sulfate from evaporites. Besides, this fluid had to interact with Ba-bearing minerals, such
530 as K-feldspars and K-micas (Hanor, 2000), which are main components within the Paleozoic
531 granodiorites and phyllites and the Miocene siliciclastics filling the Neogene basins. These fractures
532 formed after the NE-SW dolomite veins, as indicated by crosscutting relationships, but we cannot
533 settle these structures in time without any doubt. However, the compressional character of these
534 structures leads us to point out that their formation took place either during the Paleogene
535 compressional event or during the minor compressional stage that occurred during the Langhian to
536 early Serravallian. In the former case, reverse faults do not show the common NE-SW Paleogene
537 orientation, but a reactivation of previous discontinuities cannot be excluded. In the latter, reverse
538 and dextral strike-slip faults with similar orientations cemented by calcite and minor barite have been
539 identified in the Burdigalian conglomerates (Parcerisa et al., 2005; Travé and Calvet, 2001, Travé et
540 al., 2009). These calcites have similar $\delta^{18}O$ values to calcite 1 but more positive $\delta^{13}C$. The $\delta^{13}C$-
541 depletion in calcite 1, between -12.7 and -9.7 ‰VPDB, could be caused by organic matter oxidation
542 via sulfate reduction, as could be pointed by the association with barite (Sass et al., 1991), or by the
543 entrance of soil-derived CO_2 (Hudson, 1977).
544 Finally, the youngest structures identified in the Turó de les Forques correspond to NE-SW and
545 NNW-SSE normal faults affecting both Paleozoic and Miocene rocks, which form gouges and calcite
546 slickenlines, respectively (fig. 16). The formation of gouges in the NE-SW normal faults affecting
547 the phyllites clearly indicates brittle deformation at very shallow crustal levels (Sibson, 1977). Calcite
548 2 cement shows a narrow range of $\delta^{13}C$ values consistent with those of the Miocene lacustrine

549 carbonates (-7.7 to -6.5 ‰VPDB), indicating that the fluid was buffered by the Miocene lacustrine
550 carbonates (Tasse and Hesse, 1984; Marshall, 1992). On the other hand, calcite 2 cement is
551 characterized by significant $\delta^{18}O$-depleted values (fig. 6), which could result from high temperature
552 fluids or low $\delta^{18}O$ groundwaters. High temperature fluids can be ruled out since fluid inclusions in
553 calcite 2 are monophasic and therefore are interpreted to be trapped at temperatures below 50ºC
554 (Goldstein and Reynolds, 1994). Moreover, these fluid inclusion associations formed by uniquely all-
555 liquid fluid inclusions are indicative of their entrapment within the phreatic zone and the lack of
556 heating during burial (Goldstein and Reynolds, 1994). The $\delta^{18}O$ composition of the lacustrine host
557 rocks, -8‰VPDB, is consistent with the $\delta^{18}O$ composition of the Miocene meteoric waters, estimating
558 that during the Miocene the Vallès-Penedès basin was only 4º to the south of its current latitude
559 (Smith, 1996) and thus, the $\delta^{18}O$ of precipitation waters was probably similar to current precipitation
560 waters (around -7‰ SMOW, according to Plata (1994) and Redondo and Yélamos (2000)). Thus,
561 applying the equation of Craig (1965), and taking into account this depleted value for groundwaters
562 and the $\delta^{18}O$ of the calcites, a range of fluid temperatures between 34 and 57ºC is obtained. These
563 temperatures are in agreement with the maximum burial depth of Burdigalian sediments in the
564 southern Vallès-Penedès margin (up to 1 km according to Travé et al., 2009), considering a
565 geothermal gradient of 30ºC/km (Juez-Larré, 2003). Calcite 2 cement has similar isotopic values to
566 calcites cementing faults in the Burdigalian clays, sandstones and conglomerates of the surrounding
567 areas (Travé et al., 2001, 2009). These authors also interpreted these calcite cements as precipitated
568 from meteoric waters.
569
570 **8.2. Structural evolution and fracture development of the Turó de les Forques hill**
571 The Turó de les Forques hill and its associated fracture pattern resulted from a long-lived tectonic
572 history spanning from Carboniferous up to Miocene. Unlike Hercynian quartz veins, albite veins
573 (albite-quartz 3-chlorite 3±titanite-anatase) are exclusive from the Ordovician phyllites of the Turó

de les Forques. They have not been observed neither in other phyllite outcrops along the CCR nor in any study about deformation and fluids in Mesozoic and Paleozoic rocks along the CCR (Carreras and Santanach, 1975; Cardellach et al., 2002; Tucker and Marshall, 2004; Piqué et al., 2008; Baqués et al., 2012; Cantarero et al., 2014b, c). As a consequence, a specific structural control, different to other areas, had to exist in the Turó de les Forques to be the responsible of these veins. NNW-SSE normal faults were active during the early Permian extensional event (see Marzo (1979), section 8.1). One of these faults, the Llobregat Fault, limited the Turó de les Forques to the SW following the trace of the current Llobregat River (fig. 1), and constituted an important paleogeographic limit during the sedimentation of the Buntsandstein controlling its thickness (Marzo, 1979; Anadón et al., 1979). The activity of this fault during the early Permian coupled with the abundance of albite veins in the Turó de les Forques hill allow us to propose that two SW-dipping extensional fault segments, laterally offset, of the Llobregat fault (fig. 1A), generated a relay zone between the two fault tips (fig. 17A). The high fracture density, up to 75 fractures/m, and the several fracture orientations are in agreement with fracture patterns described in relay zones in order to accommodate the extension between the two fault tips (Peacock and Sanderson, 1994; Soliva and Benedicto, 2004; Crider and Peacock, 2004). In addition, the interpretation that albite veins precipitated from hydrothermal fluids, produced by the mixing between metamorphic and magmatic fluids, reinforces the interpretation of an existing relay zone during this time, as these zones are preferential pathways for ascendant fluid flow, including hydrothermal, magmatic and metamorphic fluids, and therefore for cement precipitation (Antonellini and Aydin, 1995; Rotevatn et al., 2007; Fossen and Rotevatn, 2016). Moreover, because of the low porosity and permeability of the phyllites, the hydrothermal upflow was especially focused through the relay fractures that increased the permeability. During the Mesozoic extension, two rifting stages took place in the CCR and deformation was mostly accommodated by the NE-SW faults with minor contribution of the NW-SE transverse fault system (Bartrina et al., 1992). Within the Turó de les Forques and closer areas (Martorell-1 well; fig. 1), the Mesozoic succession is absent and the Miocene

599 sediments unconformably overlays the Paleozoic rocks (Lanaja, 1987). This fact indicates that the
600 studied area remained as a structural high with no sedimentation or even erosion. The Paleogene
601 compression (middle Eocene - Oligocene) uplifted the whole CCR reactivating previously developed
602 NE-SW extensional faults (Roca, 1994). Within the studied area, this compressional stage could be
603 registered by reverse faults and associated calcite veins. Finally, during the Miocene extension, NE-
604 SW faults generated the current horst and graben geometry of the CCR, which was lately segmented
605 by the reactivation of NW-SE faults. Thus, it is during this phase that the Turó de les Forques acquired
606 its current configuration as an isolated horst (fig. 17B). The Paleozoic rocks of the horst also remained
607 poorly buried during this extensional event as revealed by the generation of gouges and the
608 precipitation of low temperature cements in the NW-SE normal faults and the thin fluvio-lacustrine
609 Burdigalian sequence (Anadón and Cabrera, 1980; Cabrera, 1981). In contrast, the Martorell-1 well
610 testifies more than 2.2 km of Miocene succession (Lanaja, 1987) denoting the important throw of the
611 NE-SW normal faults and the differential subsidence between the two near areas.
612
613 **9. Conclusions**
614 The Turó de les Forques horst, formed by Ordovician phyllites, registers a long deformation history
615 that spans from Ordovician to Miocene times that embrace from a ductile regime in the greenschist
616 facies to shallow brittle deformation.
617 Nine fracture types have been characterized in this horst. Based on petrological and geochemical
618 analyses of their mineral assemblages, the evolution of the fluid flow system was established during
619 the progressive deformation of the sequence constituting the horst:
620 (1) Syn-cleavage and post-cleavage veins of qtz_1-chl_1±mu and late qtz_2-chl_2-dol_1 formed during the
621 main Hercynian deformation. These cements precipitated from metamorphic fluids, possibly evolved
622 from seawater connate fluids, in a closed hydrological system at temperatures between 240 and

340ºC. The fluid flow system was dominated by a regional channelized system along mesoscopic veins coupled with a local pervasive system through grain boundaries and triple points.

(2) En-echelon vein arrays of ab-qtz_3-chl_3±ti-an and NE-SW normal faults generating breccias mark the change from: 1) ductile to brittle conditions, 2) compressional to extensional tectonics and 3) closed to open hydrologic regime. This paragenesis precipitated from the mixing of metamorphic and magmatic fluids, related to late-Hercynian porphyries, at temperatures between 180 and 290ºC during the early Permian extension.

(3) Dolomite veins (dol_2-chl_4-qtz_4) are possibly associated to the late stage of the early Permian extension. Vein-filling minerals precipitated at 210-280ºC from the mixing of previous fluids with hypersaline external brines in an open hydrological system at more oxidizing conditions.

(4) Reverse faults and cc1-ba veins formed either during the Paleogene compression or during the Langhian to early Serravallian minor compression. Calcite and barite precipitated from meteoric or marine waters in an open hydrological system.

(5) Finally, the Miocene extension is represented by NE-SW normal faults with fault gouges and NW-SE normal faults cemented by calcite 2 that precipitated at temperatures below 50ºC from meteoric fluids in an open basin-scale hydrological system.

The ductile to brittle transition occurred between the change from compressional to extensional tectonics in the early Permian. This transition was produced by the exhumation resulting from the uplift and erosion of the orogen during compression.

The intense albite veining, concentrated exclusively in the Turó de les Forques, together with their shear sense and orientations fits into a kinematic model of a relay ramp between two segments of the Llobregat fault. Such structure, produced during the early Permian collapse of the Hercynian orogen, produced a high-permeability path for the fast upflow of hydrothermal fluids in the low-permeability phyllites.

The outcrop of this early Permian relay zone within the Miocene horst is due to a structural and erosional control. On one hand, the successive deformation phases have reactivated inherited faults, concentrating deformation along the same structures. On the other hand, from Permian up to now, the Turó de les Forques has been a structural high due to its position at the footwall of the NW-SE Permian extensional faults and at the footwall of the NE-SW Miocene extensional faults. As a consequence, the Turó de les Forques has remained as an area of almost no sedimentation and affected by erosion, allowing the exposure of the Permian relay zone.

Acknowledgements

We thank Dr. Zhou and two anonymous referees for their constructive reviews, which helped to improve the quality of the manuscript. The isotopic, Raman, FRX, DRX and electron microprobe analyses were carried out at “Centres Científics i Tecnològics” of the Universitat de Barcelona. This research was performed within the framework of DGICYT Spanish Project CGL2015-66335-C2-1-R and the Grup Consolidat de Recerca “Geologia Sedimentària” (2014SGR-251).

References

Anadón, P., Colombo, F., Esteban, M., Marzo, M., Robles, S., Santanach, P., Solé Sugrañés, Ll., 1979. Evolución tectonoestratigráfica de los Catalánides. Acta Geol. Hisp.. Homenatge a Lluís Solé i Sabarís 14, 242-270.

Anadón, P., Cabrera L., 1980. Características de los depósitos lacustres y facies asociadas del Burdigaliense (Mioceno inferior) de la cuenca del Vallès-Penedès. IX Congreso Nacional de Sedimenología, Salamanca, Spain, pp. 261-276.

Anderson, R., Graham, C.M., Boyce, A.J., Fallick, A.E., 2004. Metamorphic and basin fluids in quartz-carbonate-sulphide veins in the SW Scottish Highlands: A stable isotope and fluid inclusion study. Geofluids 4, 169–185. doi:10.1111/j.1468-8115.2004.00080.x

672 Antonellini, M., Aydin, A., 1995. Effect of faulting on fluid flow in porous sandstones: Geometry
673 and spatial distribution. AAPG Bull. 79, 642–671. doi:10.1306/8D2B1B60-171E-11D7-
674 8645000102C1865D

675 Arthaud, F., Matte, P., 1977. Late Paleozoic strike-slip faulting in southern Europe and northern
676 Africa: Result of a right-lateral shear zone between the Appalachians and the Urals. GSA Bull. 88,
677 1305–1320. doi:10.1130/0016-7606(1977)88<1305:LPSFIS>2.0.CO;2

678 Aydin, A., 2000. Fractures, faults, and hydrocarbon entrapment, migration and flow. Mar. Petrol.
679 Geol. 17 (7), 797-814.

680 Baqués, V., Travé, A., Benedicto, A., Labaume, P., Cantarero, I., 2010. Relationships between
681 carbonate fault rocks and fluid flow regime during propagation of the Neogene extensional faults of
682 the Penedès basin (Catalan Coastal Ranges, NE Spain). J. Geochem. Explor. 106, 24–33.
683 doi:10.1016/j.gexplo.2009.11.010

684 Baqués, V., Travé, A., Roca, E., Marín, M., Cantarero, I., 2012. Geofluid behaviour in successive
685 extensional and compressional events : a case study from the southwestern end of the Vallès-Penedès
686 Fault (Catalan Coastal Ranges, NE Spain). Petrol. Geosci. 18, 17–31. doi: 10.1144/1354-079311-017

687 Barnaby, R.J., Rimstidt, J.D., 1989. Redox conditions of calcite cementation interpreted from Mn and
688 Fe contents of authigenic calcite. GSA Bull. 101, 795–804. doi:10.1130/0016-
689 7606(1989)101<0795:RCOCCI>2.3.CO

690 Bartrina, M.T., Cabrera, L., Jurado, M.J., Guimerà, J., Roca, E., 1992. Evolution of the central Catalan
691 margin of the Valencia trough (western Mediterranean). Tectonophys. 203, 219–247.

692 Berman, R.G., 1991. Thermobarometry using multi-equilibrium calculations; a new technique, with
693 petrological applications. Can. Mineral. 29, 833–855.

694 Berwouts, I., Van Noorden, M., Muchez, P., Boyce, A.J., Sintubin, M., 2008. Inferring intermediate-
695 scale fluid flow in a heterogeneous metasedimentary multilayer sequence during progressive

696 deformation: Evidence from the Monts d'Arrée slate belt (Brittany, France). Geofluids 8, 143–158.
697 doi:10.1111/j.1468-8123.2008.00213.x

698 Birtel, S., Stöckhert, B., 2008. Quartz veins record earthquake-related brittle failure and short term
699 ductile flow in the deep crust. Tectonophys. 457, 53–63. doi:10.1016/j.tecto.2008.05.018

700 Bodnar, R.J., 1993. Revised equation and table for determining the freezing point depression of H2O-
701 NaCl solutions. Geochim. Cosmochim. Acta 57, 683–684. doi:10.1016/0016-7037(93)90378-A

702 Cabrera, L., 1981. Influencia de la tectónica en la sedimentación continental de la cuenca del Valles-
703 Penedes (provincia de Barcelona , España) durante el Mioceno inferior. Acta Geol. Hisp. 16, 165–
704 171.

705 Cantarero, I., Lanari, P., Vidal, O., Alías, G., Travé, A., Baqués, V., 2012. Evolution of the Vallès
706 fault from chlorite and mica equilibrium. Geo-Temas 13, 770–773.

707 Cantarero, I., Zafra, C.J., Travé, A., Martín-martín, J.D., Baqués, V., Playà, E., 2014a. Fracturing and
708 cementation of shallow buried Miocene proximal alluvial fan deposits. Mar. Petrol. Geol. 55, 87–99.

709 Cantarero, I., Lanari, P., Vidal, O., Alías, G., Travé, A., Baqués, V., 2014b. Long-term fluid
710 circulation in extensional faults in the central Catalan Coastal Ranges: P–T constraints from
711 neoformed chlorite and K-white mica. Int. J. Earth Sci. 103, 165–188. doi:10.1007/s00531-013-0963-
712 8

713 Cantarero, I., Travé, a., Alías, G., Baqués, V., 2014c. Polyphasic hydrothermal and meteoric fluid
714 regimes during the growth of a segmented fault involving crystalline and carbonate rocks (Barcelona
715 Plain, NE Spain). Geofluids 14, 20–44. doi:10.1111/gfl.12021

716 Cardellach, E., Canals, À., Grandia, F., 2003. Recurrent hydrothermal activity induced by successive
717 extensional episodes: The case of the Berta F-(Pb-Zn) vein system (NE Spain). Ore Geol. Rev. 22,
718 133–141. doi:10.1016/S0169-1368(02)00112-9

719 Carreras, J., Santanach, P., 1975. Precisiones acerca de la significación petrológica y estructural de
720 las rocas gneísicas y cataclásticas del Maresme (prov. de Barcelona). Acta Geol. Hisp. X, 49–54.

721 Connolly, J.A.D., 1997. Devolatilization-generated fluid pressure and deformation-propagated fluid
722 flow during prograde regional metamorphism. J. Geophys. Res. 102, 18149–18173.
723 doi:10.1029/97jb00731

724 Connolly, J.A.D., 2010. The mechanics of metamorphic fluid expulsion. Elements 6, 165-172.
725 doi:10.2113/gselements.6.3.165

726 Craig, H., 1965. The measurements of oxygen isotope paleotemperatures. In: Tongiorgi, E. (Ed.),
727 Stable Isotopes in Oceanographic Studies and Paleotemperatures. Consiglio Nazionale delle
728 Richerche, Laboratorio di Geologia Nucleare, Pisa, pp. 161-182.

729 Crider, J.G., Peacock, D.C.P., 2004. Initiation of brittle faults in the upper crust: A review of field
730 observations. J. Struct. Geol. 26, 691–707. doi:10.1016/j.jsg.2003.07.007

731 Cruset, D., Cantarero, I., Travé, A., Vergés, J., John, C.M., 2016. Crestal graben fluid evolution
732 during growth of the Puig-reig anticline (South Pyrenean fold and thrust belt). J. Geodyn. 101, 30–
733 50. doi:10.1016/j.jog.2016.05.004

734 Dee, S.J., Roberts, S., 1993. Late-Kinematic Gold Mineralization during Regional Uplift and the Role
735 of Nitrogen - an Example from the La Codosera Area, W Spain. Mineral. Mag. 57, 437–450.

736 Deming, D., 1994. Fluid flow and heat transport in the upper continental crust. In: Parnell, J. (Ed.),
737 Geofluids: Origin, Migration and Evolution of Fluids in Sedimentary Basins, Geological Society
738 Special Publication. pp. 27–42.

739 Depoorter, S., Jacques, D., Piessens, K., Muchez, P., and Sintubin, M., 2014. The Mousny massive
740 quartz occurrence - the vestige of a late-orogenic dilational jog in the High-Ardenne slate belt
741 (Belgium). Geol. Belg. 17 (3-4), 293-310.

742 Deroin, J.P., 2003. Le bassin permien de Blanzy-le-Creusot et ses bordures carbonifères. Bull. Inf.
743 Geol. Bassin Paris 40, 3-28.

744 Dewaele, S., Muchez, P., Banks, D.A., 2004. Fluid evolution along multistage composite fault
745 systems at the southern margin of the Lower Palaeozoic Anglo-Brabant fold belt, Belgium. Geofluids
746 4, 341–356. doi:10.1111/j.1468-8123.2004.00096.x

747 Dubacq, B., Vidal, O., de Andrade, V., 2010. Dehydration of dioctahedral aluminous phyllosilicates:
748 Thermodynamic modelling and implications for thermobarometric estimates. Contrib. Mineral.
749 Petrol. 159, 159–174. doi:10.1007/s00410-009-0421-6

750 Duddy, I.R., Green, P.F., Bray, R.J., Hegarty, K.A., 1994. Recognition of the thermal effects of fluid
751 flow in sedimentary basins. In: Parnell, J. (Ed.), Geofluids: Origin, Migration and Evolution of Fluids
752 in Sedimentary Basins. Geological Society Special Publication 78, pp. 325-345.

753 Enrique, P., 1990. The Hercynian intrusive rocks of the Catalonian Coastal Ranges (NE Spain). Acta
754 Geol. Hisp. 25, 39–64.

755 Faure, M., 1995. Late orogenic carboniferous extensions in the Variscan French Massif Central.
756 Tectonics 14, 132–153. doi:10.1029/94TC02021

757 Ferry, J.M., Dipple, G.M., 1991. Fluid flow, mineral reactions, and metasomatism. Geology 19, 211–
758 214.

759 Fossen, H., Rotevatn, A., 2016. Fault linkage and relay structures in extensional settings-A review.
760 Earth-Science Rev. 154, 14–28. doi:10.1016/j.earscirev.2015.11.014

761 Foster, M.D., 1962. Interpretation of the composition and a classification of the chlorites. US
762 Geological Survey Professional Paper 414-A, 1-33.

763 Fritz, P., Smith, D.G.W., 1970. The isotopic composition of secondary dolomites. Geochim.
764 Cosmochim. Acta 34, 1161–1173. doi:10.1016/0016-7037(70)90056-6

765 Fyfe, W.S., Price, N.J., Thompson, A.B., 1978. Fluids in the Earth's crust. Their significance in
766 metamorphic, tectonic and chemical transport processes. Developments in geochemistry 1. Elsevier
767 Scientific Publishing Company, Amsterdam, 383 p.

768 Garven, G., 1989. A hydrogeologic model for the formation of the giant oil sands deposits of the
769 western Canada sedimentary basin. Am. J. Sci. 289, 105-166.

770 Gaspar-Escribano, J.M., Garcia-Castellanos, D., Roca, E., Cloetingh, S., 2004. Cenozoic vertical
771 motions of the Catalan Coastal Ranges (NE Spain): The role of tectonics, isostasy, and surface
772 transport. Tectonics 23, TC1004. doi:10.1029/2003TC001511

773 Ghisetti, F., Kirschner, D.L., Vezzani, L., Agosta, F., 2001. Stable isotope evidence for contrasting
774 paleofluid circulation in thrust faults and normal faults of the central Apennines, Italy. J. Geophys.
775 Res. 106, 8811–8825. doi:10.1029/2000JB900377

776 Gil Ibarguchi, J.I., Julivert, M., 1988. Petrología de la aureola metamórfica de la granodiorita de
777 Barcelona en la sierra de Collcerola (Tibidabo). Est. Geol. 44, 353–374.

778 Goldstein, R.H., Reynolds, T.J., 1994. Systematics of fluid inclusions in diagenetic minerals. SEPM
779 Short. Course Notes 31, 198.

780 Gómez-Gras, D., Ferrer, C., 1999. Caracterización petrológica de perfiles de meteorización antiguos
781 desarrollados en granitos tardihercínicos de la Cordillera Costero Catalana. Rev. Soc. Geol. España
782 12, 281–299.

783 Guimerà, J., 1984. Palaeogene evolution of deformation in the northeastern Iberian Peninsula. Geol.
784 Mag. 121 (5), 413-420.

785 Hanor, J.S., 2000. Barite-Celestine Geochemistry and Environments of Formation. Rev. Mineral.
786 Geochem. 40, 193–275. doi:10.2138/rmg.2000.40.4

787 Hanor, J.S., 1994. Origin of saline fluids in sedimentary basins, in: Geofluids: Origin, Migration and
788 Evolution of Fluids in Sedimentary Basins, Geological Society Special Publication. pp. 151–174.
789 doi:10.1144/GSL.SP.1994.078.01.13

790 Heinrich, C.A., 2005. The physical and chemical evolution of low-salinity magmatic fluids at the
791 porphyry to epithermal transition: A thermodynamic study. Miner. Depos. 39, 864–889.
792 doi:10.1007/s00126-004-0461-9

793 Hudson, J.D., 1977. Stable isotopes and limestone lithification. J. Geol. Soc. London. 133, 637–660.
794 doi:10.1144/gsjgs.133.6.0637

795 Imber, J., Holdsworth, R.E., Butler, C.A., 2001. A reappraisal of the Sibson-Scholz fault zone model:
796 the nature of the frictional to viscous ("brittle-ductile") transition along a long-lived, crustal-scale
797 fault, Outer Hebrides, Scotland. Tectonics 20, 601–624.

798 Juez-Larré, J., 2003. Post Late Paleozoic tectonothermal evolution of the northeastern margin of
799 Iberia, assessed by fission-track and (U-Th)/He analyses. A case history from the Catalan Coastal
800 Ranges. Ph.D. Thesis, Vrije Universiteit, Amsterdam.

801 Julivert, M., Duran, H., 1990a. The Hercynian structure of the Catalonian Coastal Ranges (NE Spain).
802 Acta Geol. Hisp. 25, 13–21.

803 Julivert, M., Duran, H., 1990b. Paleozoic stratigraphy of the Central and Northern part of the
804 Catalonian Coastal Ranges (NE Spain). Acta Geol. Hisp. 25, 3–12.

805 Kenis, I., Muchez, P., Verhaert, G., Boyce, A. J., and Sintubin, M., 2005. Fluid evolution during
806 burial and Variscan deformation in the Lower Devonian rocks of the High-Ardenne slate belt
807 (Belgium): sources and causes of high-salinity and C-O-H-N fluids. Contrib. Mineral. Petrol. 150,
808 102-118.

809 Kruhl, J.H., Wirth, R., Morales, L.F.G., 2013. Quartz grain boundaries as fluid pathways in
810 metamorphic rocks. J. Geophys. Res. 118, 1957–1967. doi:10.1002/jgrb.50099

Labaume, P., Moretti, I., 2001. Diagenesis-dependence of cataclastic thrust fault zone sealing in sandstones. Example from the Bolivian Sub-Andean Zone. J. Struct. Geol. 23, 1659–1675. doi:10.1016/S0191-8141(01)00024-4

Lacroix, B., Charpentier, D., Buatier, M., Vennemann, T., Labaume, P., Adatte, T., Travé, A., Dubois, M., 2012. Formation of chlorite during thrust fault reactivation. Record of fluid origin and P-T conditions in the Monte Perdido thrust fault (southern Pyrenees). Contrib. Mineral. Petrol. 163, 1083–1102. doi:10.1007/s00410-011-0718-0

Lago, M., Arranz, E., Pocoví, A., Galé, C., Gil-Imaz, A., 2004. Permian magmatism and basin dynamics in the southern Pyrenees: a record of the transition from late Variscan transtension to the early Alpine extension. In: Wilson, M., Neumann, E., Davies, G., Timmerman, M., Heeremans, M., Larsen, B. (Eds.), Permo-Carboniferous Magmatism and Rifting in Europe. Geological Society, London, Special Publications. pp. 439–464. doi:10.1144/gsl.sp.2004.223.01.19

Lanaja, J. M., 1987. Contribución de la exploración petrolífera al conocimiento de la Geología de España. IGME, Ministerio Industria Energía, Madrid. 465 pp.

Lanari, P., Guillot, S., Schwartz, S., Vidal, O., Tricart, P., Riel, N., Beyssac, O., 2012. Diachronous evolution of the alpine continental subduction wedge: Evidence from P-T estimates in the Briançonnais Zone houillère (France - Western Alps). J. Geodyn. 56–57, 39–54. doi:10.1016/j.jog.2011.09.006

Lanari, P., 2012. Micro-cartographie P-T-e dans les roches métamorphiques Applications aux Alpes et à l'Himalaya. Ph.D. Thesis, Université de Grenoble, France.

Lanari, P., Wagner, T., Vidal, O., 2014. A thermodynamic model for di-trioctahedral chlorite from experimental and natural data in the system MgO-FeO-Al_2O_3-SiO_2-H_2O: Applications to P-T sections and geothermometry. Contrib. Mineral. Petrol. 167, 1–19. doi:10.1007/s00410-014-0968-8

834 Marquer, D., Burkhard, M., 1992. Fluid circulation, progressive deformation and mass-transfer
835 processes in the upper crust: the example of basement-cover relationships in the External Crystalline
836 Massifs, Switzerland. J. Struct. Geol. 14, 1047–1057. doi:10.1016/0191-8141(92)90035-U

837 Marshall, J.D., 1992. Climatic and oceanographic isotopic signals from the carbonate rock record and
838 their preservation. Geol. Mag. 129, 143. doi:10.1017/S0016756800008244

839 Martínez, F.J., Dietsch, C., Aleinikoff, J., Cirés, J., Arboleya, M.L., Reche, J., Gómez-Gras, D., 2016.
840 Provenance, age, and tectonic evolution of Variscan flysch, southeastern France and northeastern
841 Spain, based on zircon geochronology. GSA Bull. 128, 842–859. doi:10.1130/B31316.1

842 Marzo, M., 1979. El Bundsandstein de los Catalánides: Estratigrafía y procesos sedimentarios. Ph.D.
843 Thesis, Universitat de Barcelona, Spain.

844 Matte, P., 2001. The Variscan collage and orogeny (480 ± 290 Ma) and the tectonic de definition of
845 the Armorica microplate : a review. Terra Nova 13, 122–128.

846 McCrea, J.M., 1950. On the isotopic chemistry of carbonates and a paleotemperature scale. J. Chem.
847 Phys. 18, 849–857. doi:10.1063/1.1747785

848 Mikucki, E.J., Ridley, J.R., 1993. The hydrothermal fluid of Archaean lode-gold deposits at different
849 metamorphic grade: compositional constraints from ore and wallrock alteration assemblages. Miner.
850 Depos. 28, 469–481.

851 Miller, J. a, Cartwright, I., 2006. Albite vein formation during exhumation of high-pressure terranes:
852 a case study from alpine Corsica. J. Metamorph. Geol. 24, 409–428. doi:10.1111/j.1525-
853 1314.2006.00645.x

854 Moore, C.H., 1989. Carbonate diagenesis and porosity. Developments in Sedimentology 46. Elsevier,
855 pp. 338.

856 Nesbitt, B.E., Muehlenbachs, K., 1989. Origins and movement of fluids during deformation and
857 metamorphism in the Canadian Cordillera. Science 245, 733–736. doi:10.1126/science.245.4919.733

858 Oliver, N.H.S., 2001. Linking of regional and local hydrothermal systems in the mid-crust by shearing
859 and faulting. Tectonophysics 335, 147–161. doi:10.1016/S0040-1951(01)00054-3

860 Oliver, N.H.S., 1996. Review and classification of structural controls on fluid flow during regional
861 metamorphism. J. Metamorph. Geol. 14, 477–492. doi:10.1046/j.1525-1314.1996.00347.x

862 Parcerisa, D., Thiry, M., Schmitt, J.M., 2010. Albitisation related to the triassic unconformity in
863 igneous rocks of the morvan massif (France). Int. J. Earth Sci. 99, 527–544. doi:10.1007/s00531-008-
864 0405-1

865 Parcerisa, D., Gómez-Gras, D., Travé, A., 2005. A model of early calcite cementation in alluvial fans:
866 Evidence from the Burdigalian sandstones and limestones of the Vallès-Penedès half-graben (NE
867 Spain). Sediment. Geol. 178, 197–217. doi:10.1016/j.sedgeo.2005.04.004

868 Parcerisa, D., Gómez-Gras, D., Travé, A., Martín-Martín, J.D., 2006. Fe and Mn in calcites cementing
869 red beds: A record of oxidation–reduction conditions. Examples from the Catalan Coastal Ranges
870 (NE Spain). J. Geochem. Explor. 89, 318–321. doi:10.1016/j.gexplo.2005.11.081

871 Parra, T., Vidal, O., Agard, P., 2002. A thermodynamic model for Fe–Mg dioctahedral K white micas
872 using data from phase-equilibrium experiments and natural pelitic assemblages. Contrib. Mineral.
873 Petrol. 143, 706–732. doi:10.1007/s00410-002-0373-6

874 Peacock, D.C.P., Sanderson, D.J., 1994. Geometry and deveopment of relay ramps in normal fault
875 systems. AAPG Bull. 78, 147–165. doi:10.1306/BDFF9046-1718-11D7-8645000102C1865D

876 Piqué, À., Canals, À., Grandia, F., Banks, D. A., 2008. Mesozoic fluorite veins in NE Spain record
877 regional base metal-rich brine circulation through basin and basement during extensional events.
878 Chem. Geol. 257, 139–152. doi:10.1016/j.chemgeo.2008.08.028

879 Pitcairn, I.K., Skelton, A.D.L., Broman, C., Arghe, F., Boyce, A., 2010. Structurally focused fluid
880 flow during orogenesis: the Islay Anticline, SW Highlands, Scotland. J. Geol. Soc. London. 167, 659–
881 674. doi: 10.1144/0016-76492009-135

882 Plata, A., 1994. Composición isotópica de las precipitaciones y aguas subterráneas de la Península
883 Ibérica. Centro de Estudios y Experimentación de Obras Públicas. Madrid, Pub. M-39, 1-139.

884 Putnis, A., 2002. Mineral replacement reactions: from macroscopic observations to microscopic
885 mechanisms. Mineral. Mag. 66 (5), 689-708.

886 Redondo, R., Yélamos, J.G., 2000. Hidrogeoquímica convencional e isotópica de las aguas
887 carbonáticas de Cataluña. Geogaceta 28, 121-124.

888 Roca, E., 1994. La evolución geodinámica de la Cuenca Catalano-Balear y áreas adyacentes desde el
889 Mesozoico hasta la actualidad. Acta Geol. Hisp. 29, 3–25.

890 Roca, E., Guimerà, J., 1992. The Neogene structure of the eastern Iberian margin - structural
891 constraints on the crustal evolution of the Valencia trough (Western Mediterranean). Tectonophys.
892 203, 203–218. doi:10.1016/0040-1951(92)90224-T

893 Rotevatn, A., Fossen, H., Hesthammer, J., Aas, T.E., Howell, J.A., 2007. Are relay ramps conduits
894 for fluid flow? Structural analysis of a relay ramp in Arches National Park, Utah. In: Lonergan, L.,
895 Jolly, R.J.H., Rawnsley, K., Sanderson, D.J. (Eds.), Fractured Reservoirs. Geological Society,
896 London, Special Publications. pp. 55–71. doi:10.1144/GSL.SP.2007.270.01.04

897 Rumble III, D., Duke, E.F., Hoering, T.L., 1986. Hydrothermal graphite in New Hampshire: evidence
898 of carbon mobility during regional metamorphism. Geology 14, 452–455. doi:10.1130/0091-
899 7613(1986)14<452:HGINHE>2.0.CO;2

900 Salas, R., Guimerà, J., Mas, R., Martín-Closas, C., Meléndez, A., Alonso, A., 2001. Evolution of the
901 Mesozoic Central Iberian Rift System and its Cainozoic inversion (Iberian chain). In: Ziegler, P.A.,

902 Cavazza, W., Robertson, A.H.F., Crasquin-Soleau, S. (Eds.), Peri-Tethys Memoir 6: Peri-Tethyan
903 Rift/Wrench Basins and Passive Margins. Mém. Mus. natn. Hist. nat. pp. 145–186.

904 Santanach, P., Casas, J.M., Gratacós, O., Liesa, M., Muñoz, J.A., Sàbat, F., 2011. Variscan and
905 Alpine structure of the hills of Barcelona : geology in an urban area. J. Iber. Geol. 37, 121–136.
906 doi:10.5209/rev

907 Sass, E., Bein, A., Almogi-Labin, A., 1991. Oxygen-isotope composition of diagenetic calcite in
908 organic-rich rocks: evidence for 18O depletion in marine anaerobic pore water. Geology 19, 839–
909 842. doi:10.1130/0091-7613(1991)019<0839:OICODC>2.3.CO

910 Shepherd, T.J., Bottrell, S.H., Miller, M.F., 1991. Fluid inclusion volatiles as an exploration guide to
911 black shale-hosted gold deposits, Dolgellau gold belt, North Wales, UK. J. Geochem. Explor. 42, 5–
912 24. doi:10.1016/0375-6742(91)90058-3

913 Sibson, R.H., 1977. Fault rocks and fault mechanisms. Geol. Soc. London 133, 191-213.

914 Sibson, R.H., Scott, J., 1998. Stress/fault controls on the containment and release of overpressured
915 fluids: examples from gold-quartz vein systems in Juneau, Alaska; Victoria, Australia and Otago,
916 New Zealand. Ore Geol. Rev. 13, 293-306.

917 Smith, A.G., 1996. Cenozoic latitudes, positions and topography of the Iberian Peninsula. In: Friend,
918 P.F., Dabrio, C.J. (Eds.), Tertiary Basins of Spain: the Stratigraphic Record of Crustal Kinematics,
919 World and Regional Geology, vol. 6. Cambridge University Press, Cambridge, pp. 6-8.

920 Smith, M., Yardley, B., 1999a. Fluid evolution during metamorphism of the Otago Schist, New
921 Zealand: (I) Evidence from fluid inclusions. J. Metamorph. Geol. 17, 173–186. doi:10.1046/j.1525-
922 1314.1999.00189.x

923 Smith, M.P., Yardley, B.W.D., 1999b. Fluid evolution during metamorphism of the Otago Schist,
924 New Zealand: (II) Influence of detrital apatite on fluid salinity. J. Metamorph. Geol. 17, 187–193.
925 doi:10.1046/j.1525-1314.1999.00190.x

926 Soliva, R., Benedicto, A., 2004. A linkage criterion for segmented normal faults. J. Struct. Geol. 26,
927 2251–2267. doi:10.1016/j.jsg.2004.06.008

928 Tasse, N., Hesse, R., 1984. Origin and significance of complex authigenic carbonates in Cretaceous
929 black shales of the Western Alps. J. Sediment. Petrol. 54, 1012-1027.

930 Taylor, Jr. H.P., 1967. Oxygen isotope studies of hydrothermal mineral deposits. In: Barnes, H.L.
931 (Ed.), Geochemistry of hydrothermal ore deposits. Holt, Rinehart and Winston, pp. 670

932 Taylor, Jr. H.P., 1977. Water/rock interactions and the origin of H_2O in granitic batholiths. J. Geol.
933 Soc. London 133, 509-558.

934 Taylor, B.E., O'Neil, J.R., 1977. Stable isotope studies of metasomatic Ca-Fe-Al-Si skarns and
935 associated metamorphic and igneous rocks, Osgood Mountains, Nevada. Contrib. Mineral. Petrol. 63,
936 1–49. doi:10.1007/BF00371674

937 Travé, A., Calvet, F., 2001. Syn-rift geofluids in fractures related to the early-middle Miocene
938 evolution of the Vallès-Penedès half-graben (NE Spain). Tectonophys. 336, 101–120.

939 Travé, A., Calvet, F., Soler, A., Labaume, P., 1998. Fracturing and fluid migration during Palaeogene
940 compression and Neogene extension in the Catalan Coastal Ranges, Spain. Sedimentology 45, 1063–
941 1082.

942 Travé, A., Roca, E., Playà, E., Parcerisa, D., Gómez-Gras, D., Martín-Martín, J.D., 2009. Migration
943 of Mn-rich fluids through normal faults and fine-grained terrigenous sediments during early
944 development of the Neogene Vallès-Penedès half-graben (NE Spain). Geofluids 9, 303–320.
945 doi:10.1111/j.1468-8123.2009.00258.x

946 Trincal, V., Lanari, P., Buatier, M., Lacroix, B., Charpentier, D., Labaume, P., Muñoz, M., 2015.
947 Temperature micro-mapping in oscillatory-zoned chlorite: Application to study of a green-schist
948 facies fault zone in the Pyrenean Axial Zone (Spain). Am. Mineral. 100, 2468–2483. doi:10.2138/am-
949 2015-5217

950 Tucker, M., Marshall, J., 2004. Diagenesis and geochemistry of Upper Muschelkalk (Triassic)
951 buildups and associated facies in Catalonia (NE. Spain): a paper dedicated to Francesc Calvet. Geol.
952 Acta 2, 257–269.

953 Van Den Kerkhof, A., Thiéry, R., 2001. Carbonic inclusions. Lithos 55, 49–68. doi:10.1016/S0024-
954 4937(00)00038-4

955 Van Noten, K., Hilgers, C., Urai, J. L., and Sintubin, M., 2008. Late burial to early tectonic quartz
956 veins in the periphery of the High-Ardenne slate belt (Rursee, North Eifel, Germany). Geol. Belg. 11
957 (3-4), 179-198.

958 Van Noten, K., Muchez, P., and Sintubin, M., 2011. Stress-state evolution of the brittle upper crust
959 during compressional tectonic inversion as defined by successive quartz vein-types (High-Ardenne
960 slate belt, Germany). J. Geol. Soc. London 168 (2), 407-422.

961 Vergés, J., García-Senz, J., 2001. Mesozoic evolution and Cainozoic inversion of the Pyrenean Rift.
962 In: Ziegler, P.A. et al. (Eds.), Peri-Tethys Memoir 6: Peri-Tethyan Rift/Wrench Basins and Passive
963 Margins. Mém. Mus. natn Hist. nat. 186, pp. 187-212.

964 Vidal, O., Dubacq, B., 2009. Thermodynamic modelling of clay dehydration, stability and
965 compositional evolution with temperature, pressure and H2O activity. Geochim. Cosmochim. Acta
966 73, 6544–6564. doi:10.1016/j.gca.2009.07.035

967 Vidal, O., De Andrade, V., Lewin, E., Munoz, M., Parra, T., Pascarelli, S., 2006. P-T-deformation-
968 Fe^{3+}/Fe^{2+} mapping at the thin section scale and comparison with XANES mapping: Application to a
969 garnet-bearing metapelite from the Sambagawa metamorphic belt (Japan). J. Metamorph. Geol. 24,
970 669–683. doi:10.1111/j.1525-1314.2006.00661.x

971 Vidal, O., Parra, T., Trotet, F., 2001. A thermodynamic model for Fe-Mg aluminous chlorite using
972 data from phase equilibrium experiments and natural pelitic assemblages in the 100° to 600°C, 1 to
973 25 kb range. Am. J. Sci. 301, 557–592. doi:10.2475/ajs.301.6.557

974 Vidal, O., Parra, T., Vieillard, P., 2005. Thermodynamic properties of the Tschermak solid solution
975 in Fe-chlorite: Application to natural examples and possible role of oxidation. Am. Mineral. 90, 347–
976 358. doi:10.2138/am.2005.1554

977 Vidal, O., Lanari, P., Muñoz, M., Bourdelle, F., de Andrade, V., 2016. Deciphering temperature,
978 pressure, and oxygen activity conditions of chlorite formation. Clay Miner. 51, 615–633.
979 doi:10.1180/claymin.2016.051.4.06

980 Vilà, M., Pin, C., 2016. Geochemistry and Nd isotope signature of the Collserola Range Palaeozoic
981 succesion (NE Iberia): Gondwana heritage and pre-Mesozoic geodynamic evolution. Geol. Mag. 153,
982 643–662. doi:10.1017/S0016756815000837

983 Walther, J. V., Orville, P.M., 1982. Volatile production and transport in regional metamorphism.
984 Contrib. Mineral. Petrol. 79, 252–257. doi:10.1007/BF00371516

985 Wood, B.J., Walther, J.V., 1986. Fluid Flow during Metamorphism and its Implications for Fluid-
986 Rock Ratios. In: Walther, J.V., Wood, B.J. (Eds), Fluid-Rock Interactions during Metamorphism.
987 Advances in Physical Geochemistry, vol 5. Springer, New York, NY

988 Yardley, B.W.D., 1986. Fluid migration and veining in the Connemara schists, Ireland. In: Walther,
989 J.V., Wood, B.J. (Eds.), Fluid–Rock Interactions during Metamorphism. Springer Verlag, New York,
990 pp. 109–131.

991 Yardley, B.W.D., 1997. The evolution of fluids through the metamorphic cycle. In: Jamtveit, B.,
992 Yardley, B.W.D. (Eds.), Fluid flow and transport in rocks: mechanisms and effects. Chapman & Hall,
993 London, pp. 99-121.

994 Yardley, B.W.D., Graham, J.T., 2002. The origins of salinity in metamorphic fluids. Geofluids 2,
995 249–256. doi:10.1046/j.1468-8123.2002.00042.x

996 Zhang, R.Y., Liou, J.G., Zheng, Y.F., Fu, B., 2003. Transition of UHP eclogites to gneissic rocks of
997 low-amphibolite facies during exhumation: Evidence from the Dabie terrane, central China. Lithos
998 70, 269–291. doi:10.1016/S0024-4937(03)00102-6

999 Ziegler, P. a, 1988. Evolution of the Arctic-North Atlantic and the western Tethys, AAPG Memoir.
1000 doi:10.1306/M43478

1001 **FIGURE CAPTIONS**

1002 **Figure 1.** Geological setting. A) Location and schematic map of the Catalan Coastal Ranges and
1003 magnification of the Littoral Chain around the study area. The black square indicates the location of
1004 the Turó de les Forques. The location of the well Martorell-1 is indicated. B) Cross-section of the
1005 CCR indicated in the inset of A (from Travé et al., 2009). C) Enlargement of the squared area in the
1006 cross-section shown in B. The square marks the location of the Turó de les Forques study area (fig.
1007 2).

1008 **Figure 2.** A) Geological map and B) cross-section of the Turó de les Forques. Location of figure 3 is
1009 indicated.

1010 **Figure 3.** A) View of the main outcrop formed by the Ordovician phyllites representing the
1011 distribution and orientation of the different fracture systems. Some of the structures could only be
1012 drawn in the lower half of the outcrop due to the impossibility of access to the upper outcrop section
1013 in order to check their distribution. B) Unconformity between Ordovician phyllites and Miocene
1014 rocks displaced by NNW-SSE normal faults and detail of the calcite slickenlines in the fault plane
1015 crosscutting the unconformity. C) Lower-hemisphere equal-area stereoplots of Miocene bedding,
1016 regional foliation and the different sets of faults and veins.

1017 **Figure 4.** Field images of fractures. A) Syn-cleavage folded quartz vein. The dashed line defines the
1018 regional foliation (S_r), which defines the axial plane of the fold. B) Late-cleavage quartz vein. C) Two
1019 single en-echelon albite vein arrays, formed by sigmoidal veins. D) En-echelon albite vein array,

formed by straight veins, associated to two discrete fault planes. E) Phyllite breccia cemented by albite. F) Cataclasite associated to the strike-slip reactivation of a NE-SW normal fault. Clasts made of albite cement are highlighted by their pinkish color (red arrow). G) NE-SW Neogene normal fault with a thick fault core formed by a grey gouge.

Figure 5. Microphotographs of the Ordovician phyllites. A) Regional foliation parallel to the compositional pelitic and quartz-rich layers (cross polarized light, XPL). B) Syn-cleavage folding of the bedding, defined by quartz-rich layers (plane polarized light, PPL). C) Regional foliation defined by muscovite, chlorite and elongated quartz (XPL). D) Crenulation of the the regional foliation (PPL).

Figure 6. $\delta^{18}O$ and $\delta^{13}C$ cross-plot of the host Miocene limestones, calcite and dolomite cements.

Figure 7. Structures and paragenetic sequence of the Turó de les Forques. Black lines: structures; grey lines: faults rocks and mineral associations.

Figure 8. Microphotographs of syn-cleavage and late-cleavage quartz veins. A) Quartz 1 crystals with undulouse extinction, subgrains, lobated grain boundaries and deformation lamellae (XPL). B) Chlorite 1-muscovite vein emplaced along quartz 1 crystals boundaries (XPL). C) Recrystallization of host rock chlorites along the border with the quartz 1 vein (PPL). D) Microshear, producing grain size reduction and recrystallization, associated with quartz elongation (XPL). E) Microvein formed by clear quartz and vermicular chlorites (PPL). F) Triple points, formed between elongated quartz crystals, and cemented with dolomite 1-chlorite 2-quartz 2 association (XPL).

Figure 9. Microphotographs of albite-quartz 3-chlorite 3±titanite-anatase paragenesis. A) Vein formed by elongated quartz and minor elongated albite (PPL). B) Vein of albite crosscutting minor crenulations (PPL). C) Breccia cemented by the paragenesis albite-quartz 3-chlorite 3±titanite-anatase (PPL). D) Quartz 1-chlorite 1 vein displaced by an albite-chlorite 3 vein. Note the vermicular morphology of chlorites contained in the kaolinitized albite (PPL). E) Fibrous-radial chlorite

aggregates at the contact between the quartz 1 vein (left) and albite-quartz 3-chlorite 3 vein (right) (XPL). F) Albite vein containing several anatase crystals (XPL).

Figure 10. Microphotographs of the dolomite 2-chlorite 4-quartz 4 paragenesis. A) Dolomite 2, partially calcitized by calcite 1, filling the remaining porosity after albite precipitation in a fracture (XPL). B) Dolomite 2 and chlorite 4 veins crosscutting quartz 1 crystals (XPL). C) Dolomite 2-chlorite 4-quartz 4 vein (PPL). D) CL image of dull dolomite 2 crosscut by a later calcite 1 vein. E) Vug developed in quartz 1 crystals partially cemented by rhombic dolomite 2, chlorite 4 and pyrite (PPL). F) CL image of rhombic dolomite crystals in vugs showing a zoned cathodoluminescence.

Figure 11. Microphotographs of the calcite 1-barite paragenesis. A) Fracture cemented by a drusy mosaic of calcite 1 (XPL). B) CL image of a calcite 1 fracture showing their zoned orange pattern. C) Cataclasite formed by phyllite and albite vein clasts (red arrows) cemented by barite (PPL). D) Microfractures between quartz 1 crystals cemented by barite (red arrow) and calcite 1 (black arrow) (XPL).

Figure 12. Microphotographs of the calcite 2 cement. A-B) Plane light and CL image of calcite 2 cement in a fault plane. C-D) Plane light and CL image of calcite 2 cement in joints characterized by rounded crystals and zoned cathodoluminescence.

Figure 13. A) Classification of chlorites according to Foster (1962). B) XFe^{3+} vs. temperature estimated from Vidal et al. (2005, 2006) geothermometer. Two main trends corresponding to two redox conditions of the fluid are observed: one from a less oxidized fluid, defined by chlorites 1 to 3 (continuous line) and one from a more oxidized fluid, defined by chlorites 4 (dashed line).

Figure 14. Homogenization temperatures (T_h) from fluid inclusions obtained for quartz 1, 3 and 4 and T_h vs. T_m plot for quartz 1, 3 and 4.

Figure 15. Pervasive fluid flow during the Hercynian deformation along microshears and intercrystalline boundaries and precipitation in low-pressure areas such as triple points created between elongated quartz crystals.

Figure 16. Evolution of deformation from ductile to brittle conditions, from Carboniferous to Miocene times, and its related structures and tectonic regime, mineral paragenesis, temperature and depth conditions, fluid origin and hydrogeologic regime. Qtz: quartz, chl: chlorite, mu: muscovite, ab: albite, dol: dolomite, ti: titanite, an: anatase, cc: calcite, ba: barite.

Figure 17. Structural evolution and fracture development of the Turó de les Forques hill. A) Generation of a relay zone between the two fault segments of the Llobregat fault during the Early Permian. Metamorphic and magmatic fluids ascend along the relay zone. B) Formation of the Turó de les Forques horst during the Miocene. Meteoric waters percolated through the faults. M1: Martorell-1 well.

Figure 1

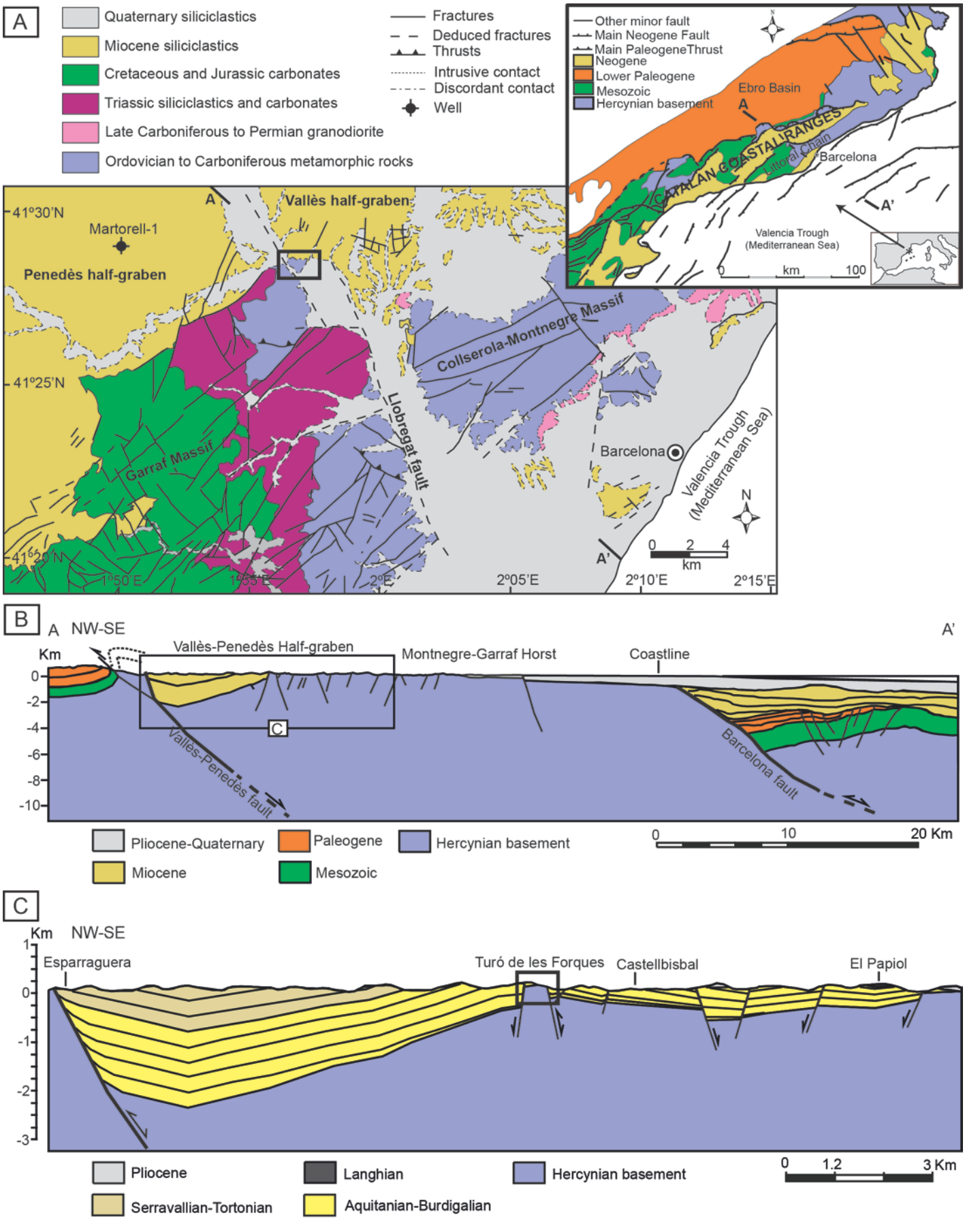
A
Quaternary siliciclastics
Miocene siliciclastics
Cretaceous and Jurassic carbonates
Triassic siliciclastics and carbonates
Late Carboniferous to Permian granodiorite
Ordovician to Carboniferous metamorphic rocks
Fractures
Deduced fractures
Thrusts
Intrusive contact
Discordant contact
Well
Other minor fault
Main Neogene Fault
Main PaleogeneThrust
Neogene
Lower Paleogene
Mesozoic
Hercynian basement
Ebro Basin
CATALAN COASTAL RANGES
Litoral Chain
Barcelona
Valencia Trough
(Mediterranean Sea)
0 km 100
41°30'N
Martorell-1
Penedès half-graben
Vallès half-graben
Collserola-Montnegre Massif
41°25'N
Garraf Massif
Llobregat fault
Barcelona
Valencia Trough
(Mediterranean Sea)
41°20'N
1°50'E
1°55'E
2°E
2°05'E
2°10'E
2°15'E
0 2 4 km
B
A NW-SE
A'
Km
Vallès-Penedès Half-graben
Montnegre-Garraf Horst
Coastline
0
-2
-4
-6
-8
-10
C
Vallès-Penedès fault
Barcelona fault
Pliocene-Quaternary
Miocene
Paleogene
Mesozoic
Hercynian basement
0 10 20 Km
C
Km NW-SE
1
0
-1
-2
-3
Esparraguera
Turó de les Forques
Castellbisbal
El Papiol
Pliocene
Serravallian-Tortonian
Langhian
Aquitanian-Burdigalian
Hercynian basement
0 1.2 3 Km

Figure 2

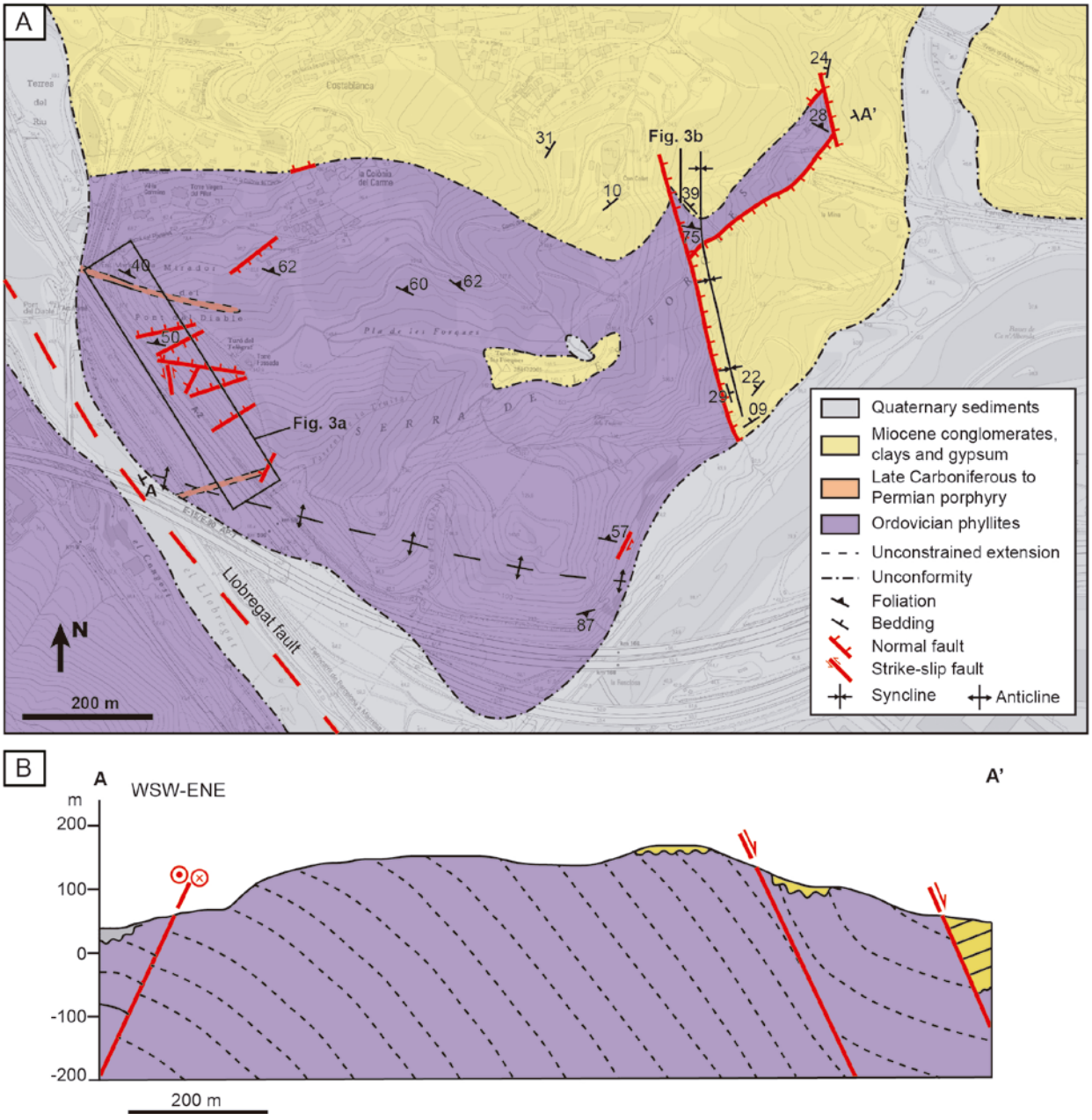
A
Fig. 3b
Fig. 3a
A'
Llobregat fault
N
200 m
Quaternary sediments
Miocene conglomerates, clays and gypsum
Late Carboniferous to Permian porphyry
Ordovician phyllites
Unconstrained extension
Unconformity
Foliation
Bedding
Normal fault
Strike-slip fault
Syncline
Anticline
B
A
WSW-ENE
A'
m
200
100
0
-100
-200
200 m

1086 Figure 3

1087

Figure 4

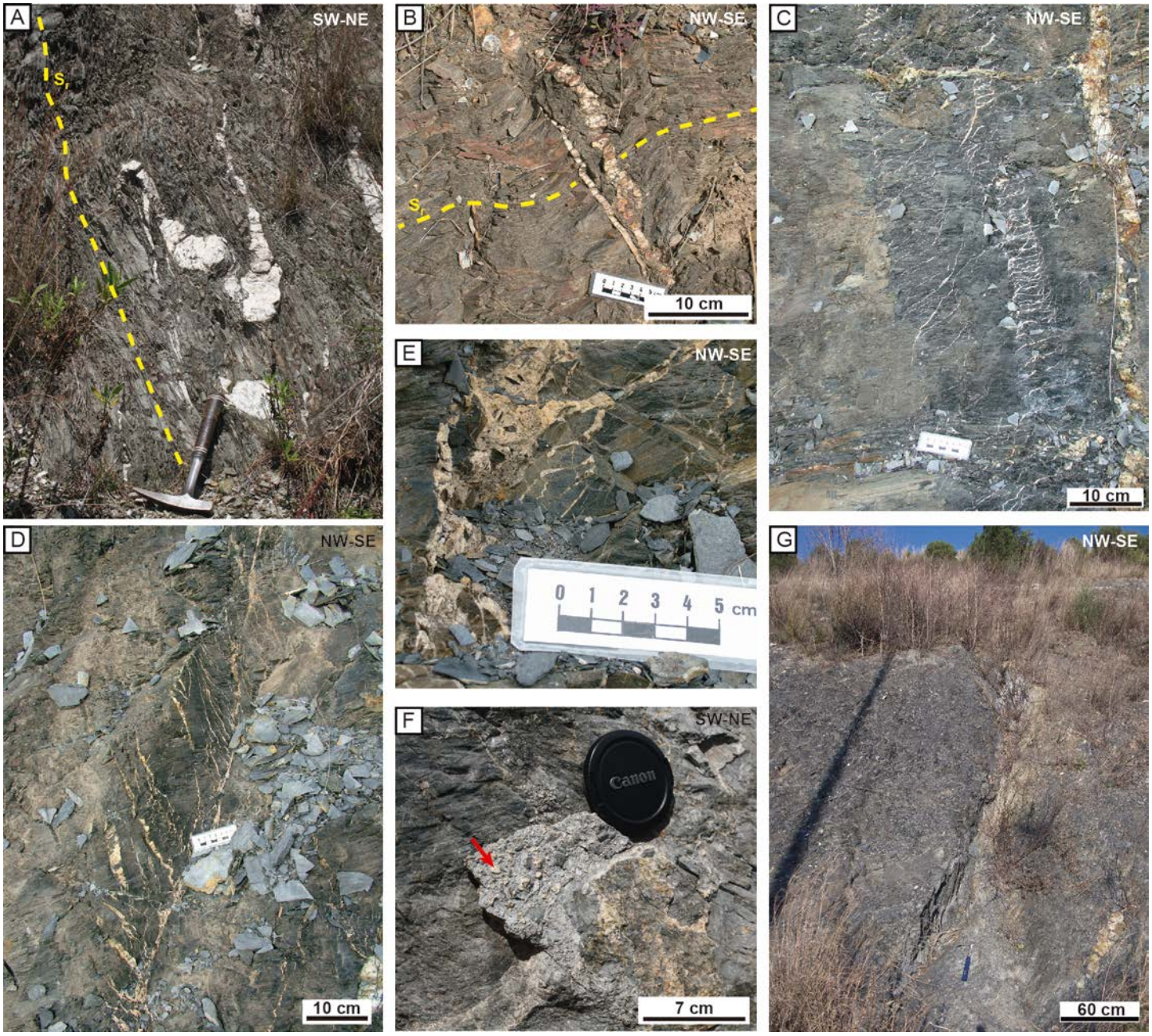
A
SW-NE
S1
B
NW-SE
S1
10 cm
C
NW-SE
10 cm
D
NW-SE
10 cm
E
NW-SE
0 1 2 3 4 5 cm
F
SW-NE
Canon
7 cm
G
NW-SE
60 cm

Figure 5

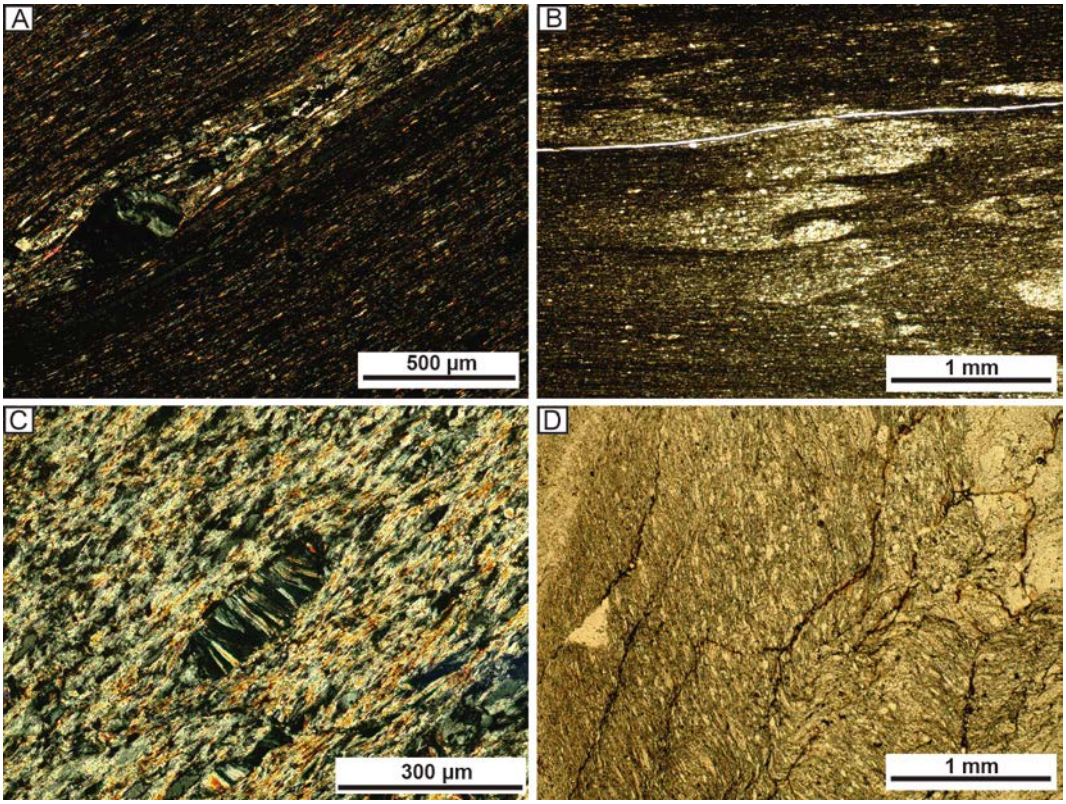

Figure 6

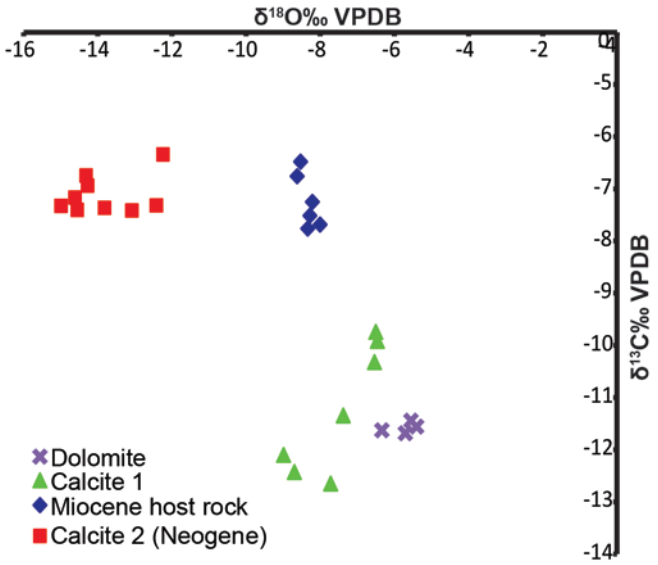
δ18O‰ VPDB
-16
-14
-12
-10
-8
-6
-4
-2
0
-5
-6
-7
-8
-9
-10
-11
-12
-13
-14
δ13C‰ VPDB
Dolomite
Calcite 1
Miocene host rock
Calcite 2 (Neogene)

Figure 7

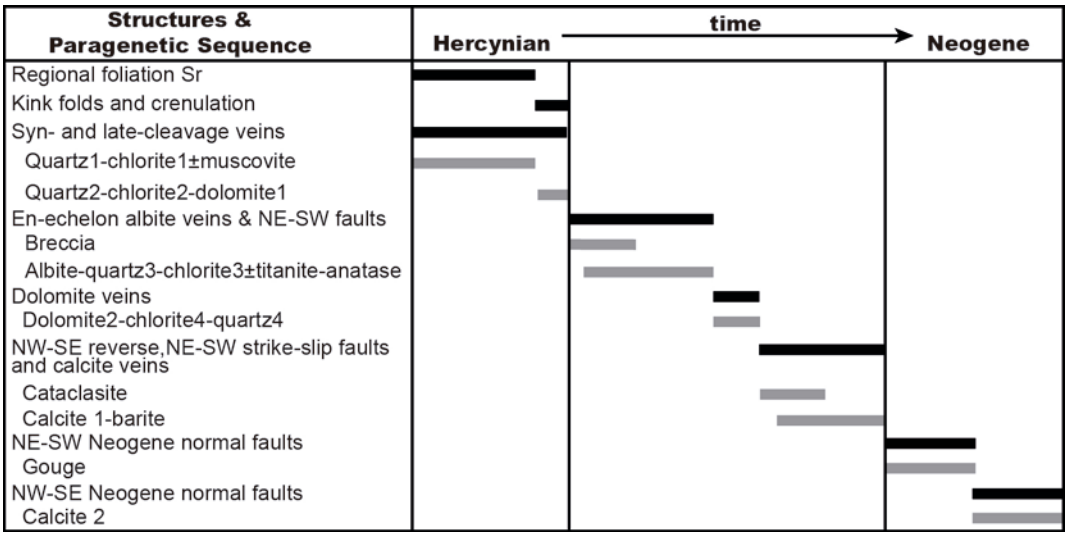
Structures &
Paragenetic Sequence
Hercynian
time
Neogene
Regional foliation Sr
Kink folds and crenulation
Syn- and late-cleavage veins
Quartz1-chlorite1±muscovite
Quartz2-chlorite2-dolomite1
En-echelon albite veins & NE-SW faults
Breccia
Albite-quartz3-chlorite3±titanite-anatase
Dolomite veins
Dolomite2-chlorite4-quartz4
NW-SE reverse,NE-SW strike-slip faults and calcite veins
Cataclasite
Calcite 1-barite
NE-SW Neogene normal faults
Gouge
NW-SE Neogene normal faults
Calcite 2

1137 Figure 8

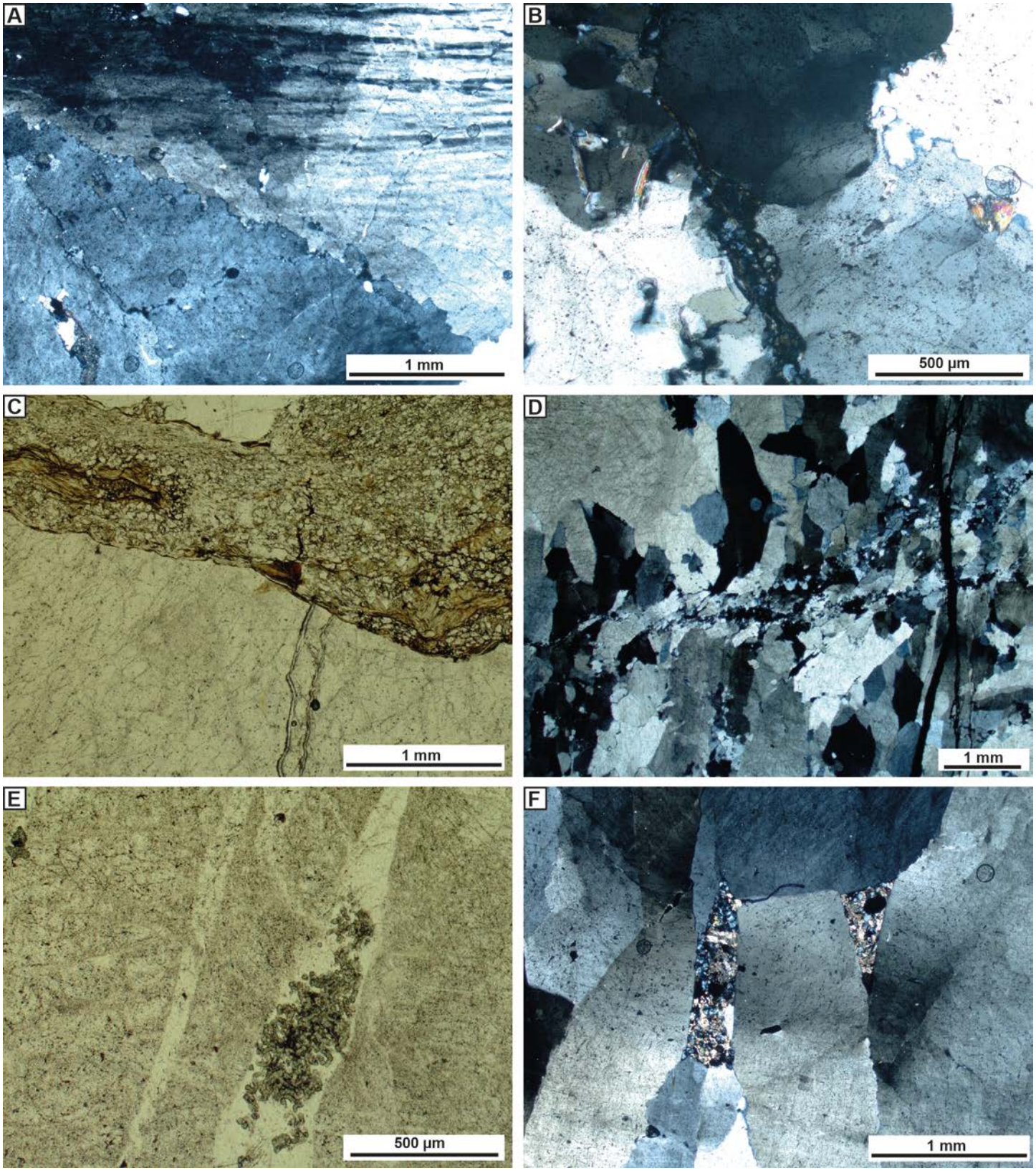

1138

1139

1140 Figure 9

1141

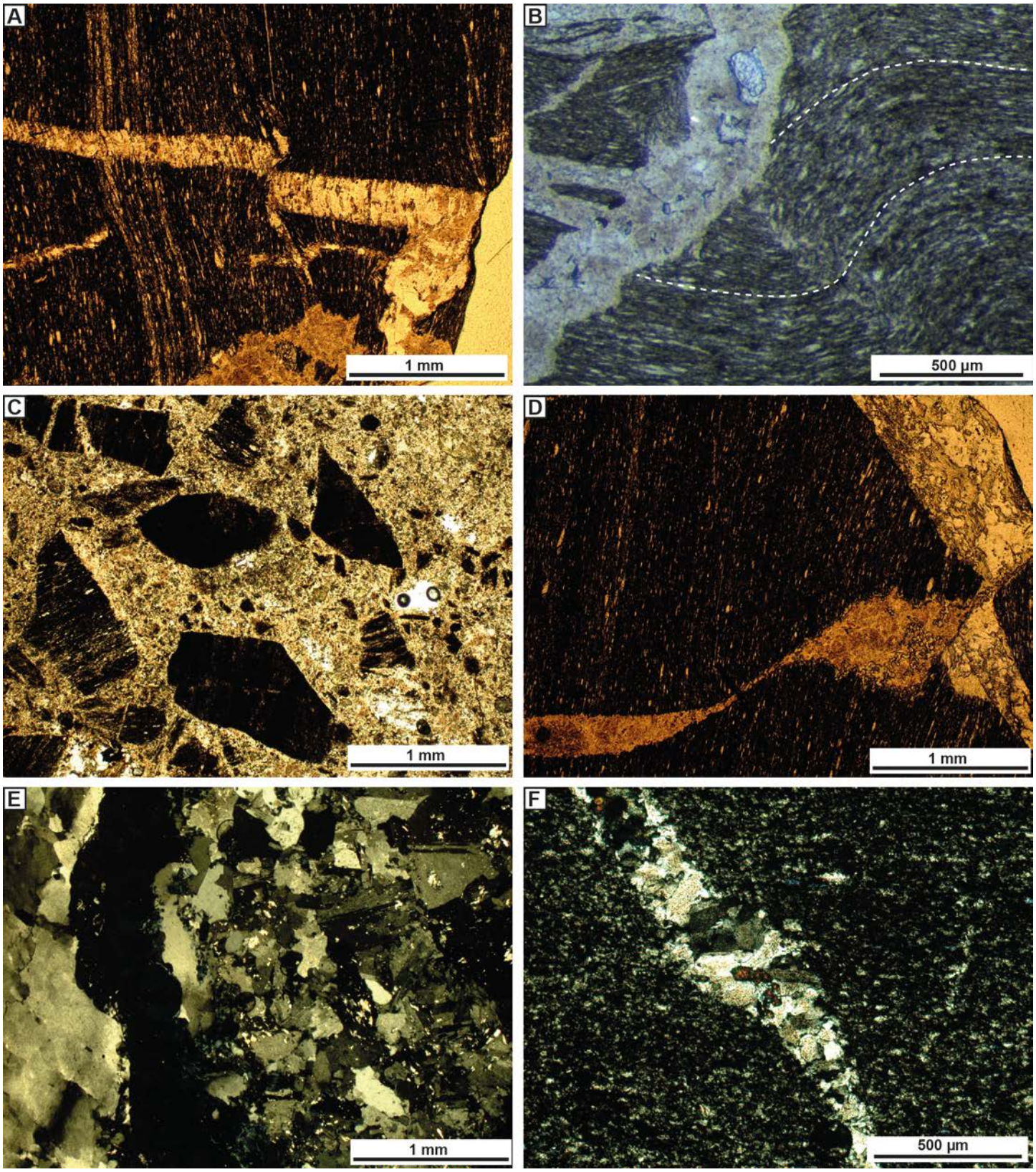

1142

Figure 10

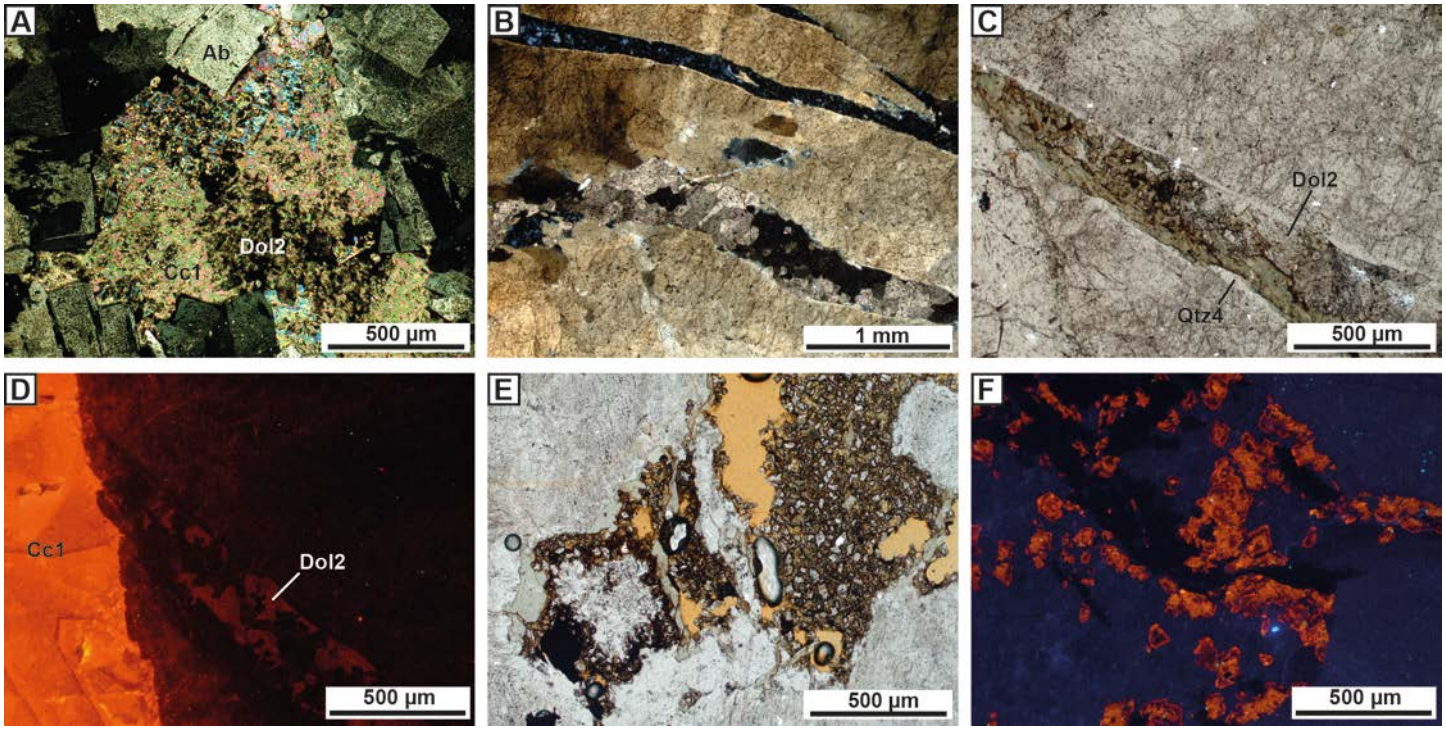
A
Ab
Dol2
Cc1
500 µm
B
1 mm
C
Dol2
Qtz4
500 µm
D
Cc1
Dol2
500 µm
E
500 µm
F
500 µm

Figure 11

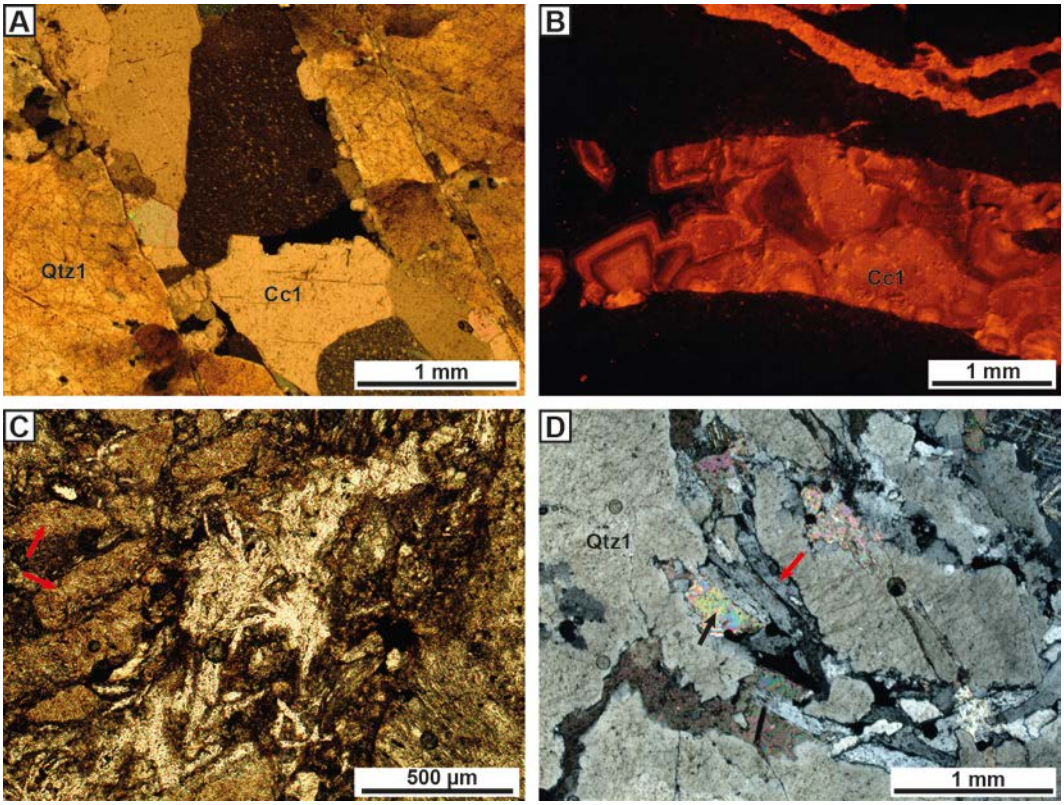

Figure 12

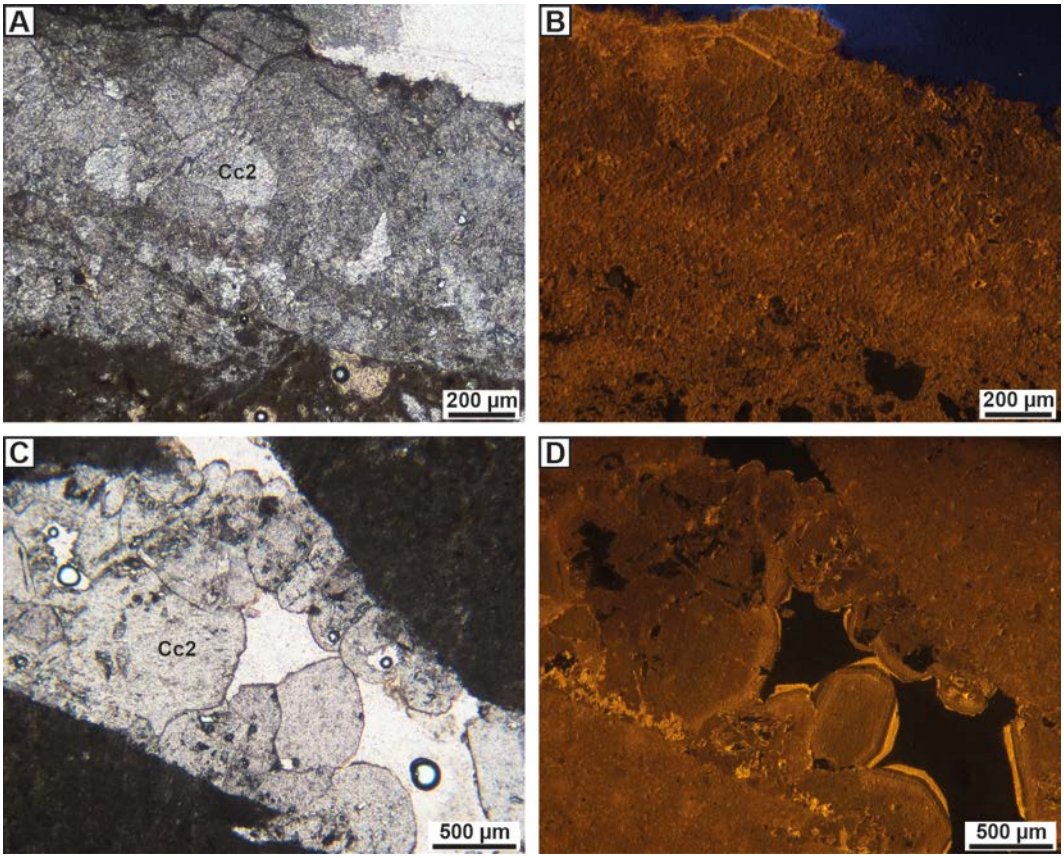

1180 Figure 13

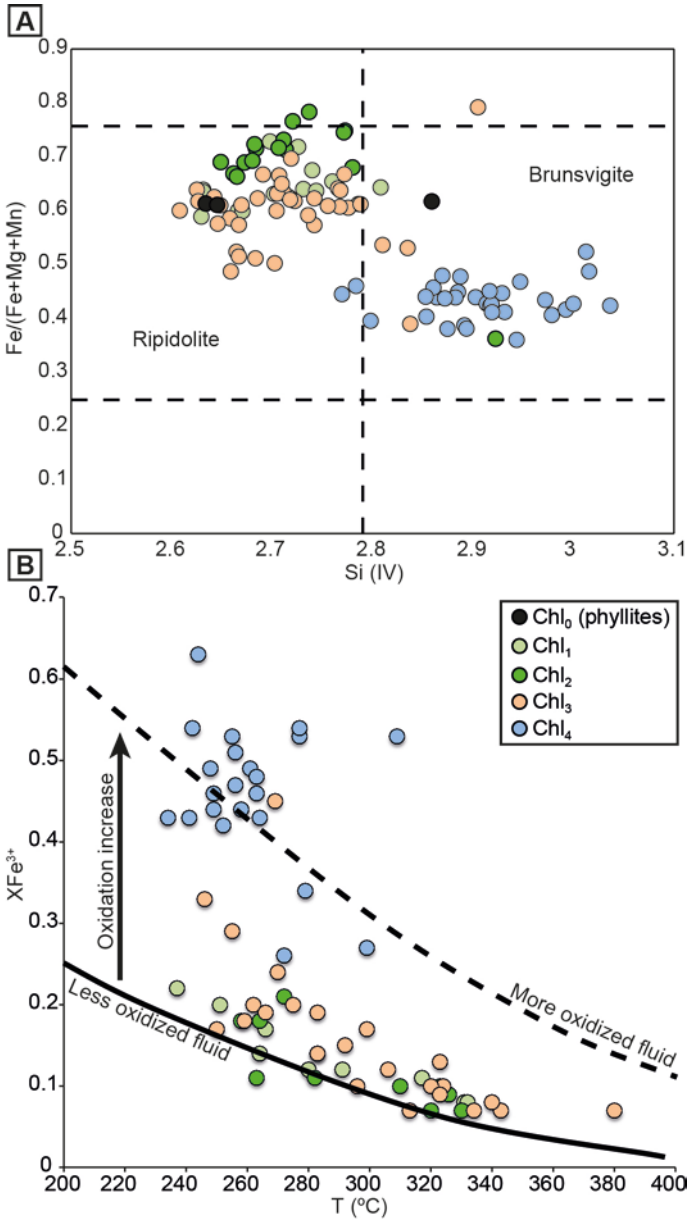

1181

1182

1183

1184

1185

1186

1187

Figure 14

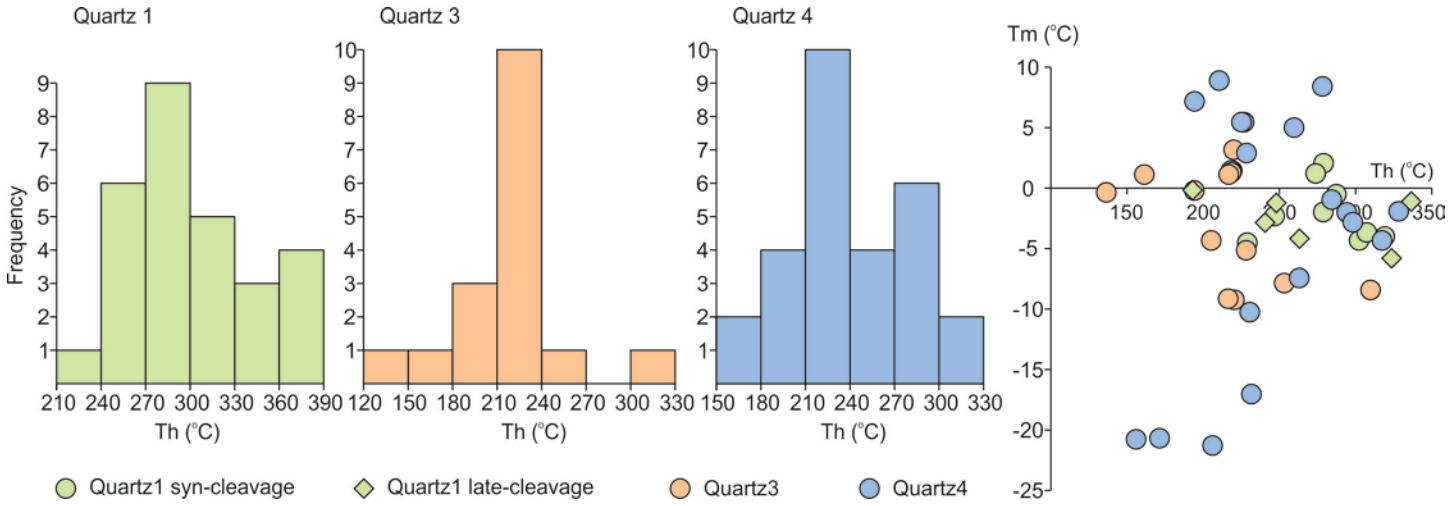
Quartz 1
Quartz 3
Quartz 4
Frequency
Th (°C)
Tm (°C)
Quartz1 syn-cleavage
Quartz1 late-cleavage
Quartz3
Quartz4

Figure 15

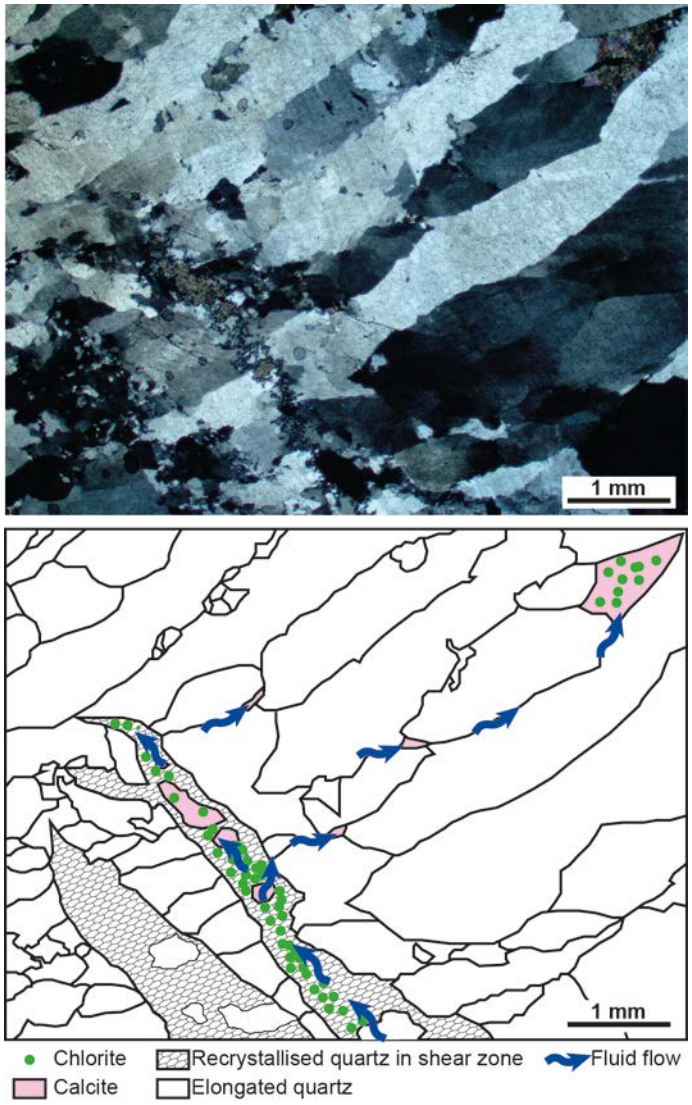
1 mm
1 mm
Chlorite
Calcite
Recrystallised quartz in shear zone
Elongated quartz
Fluid flow

1213 Figure 16

1214

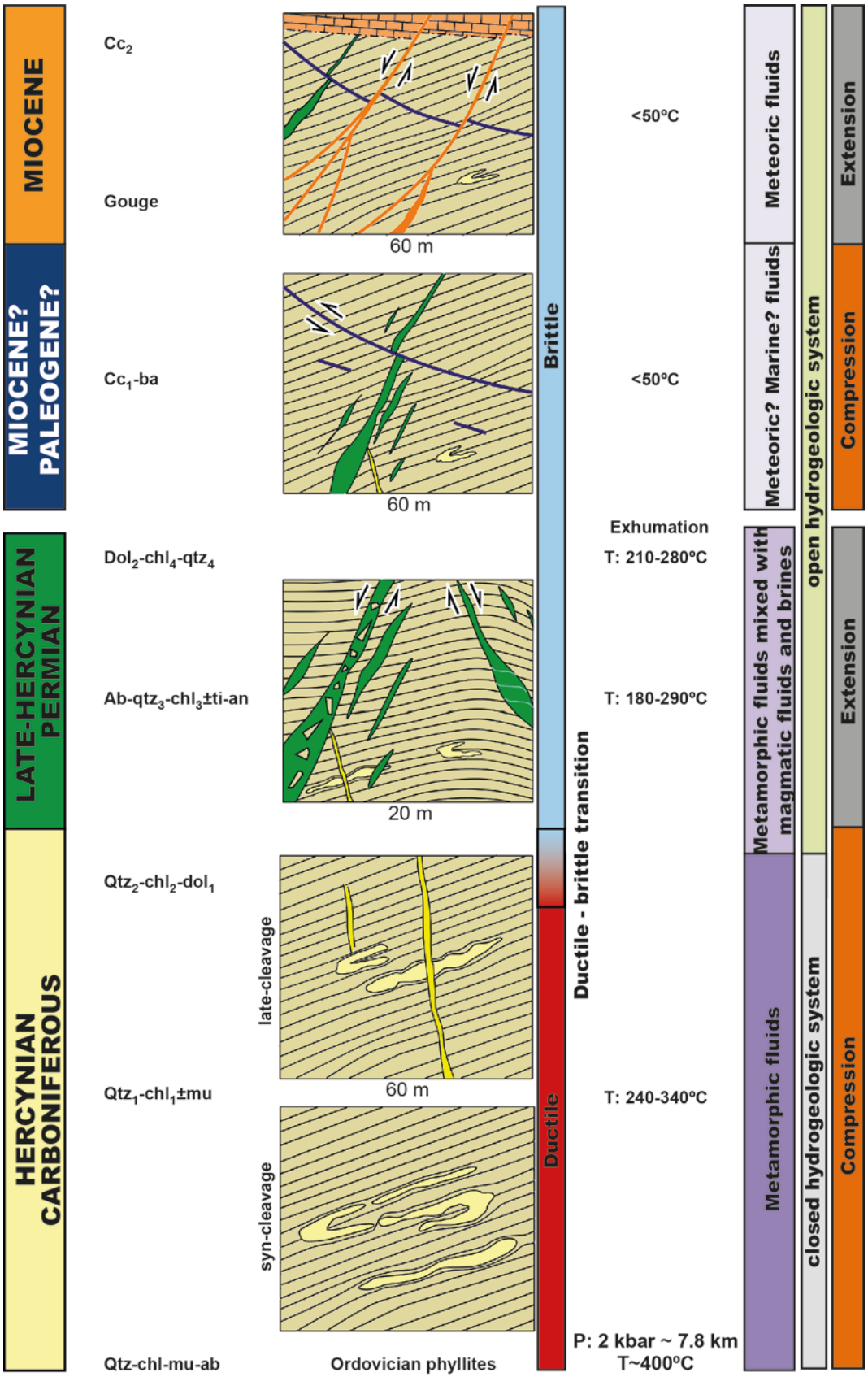

1215

1216 Figure 17

1217

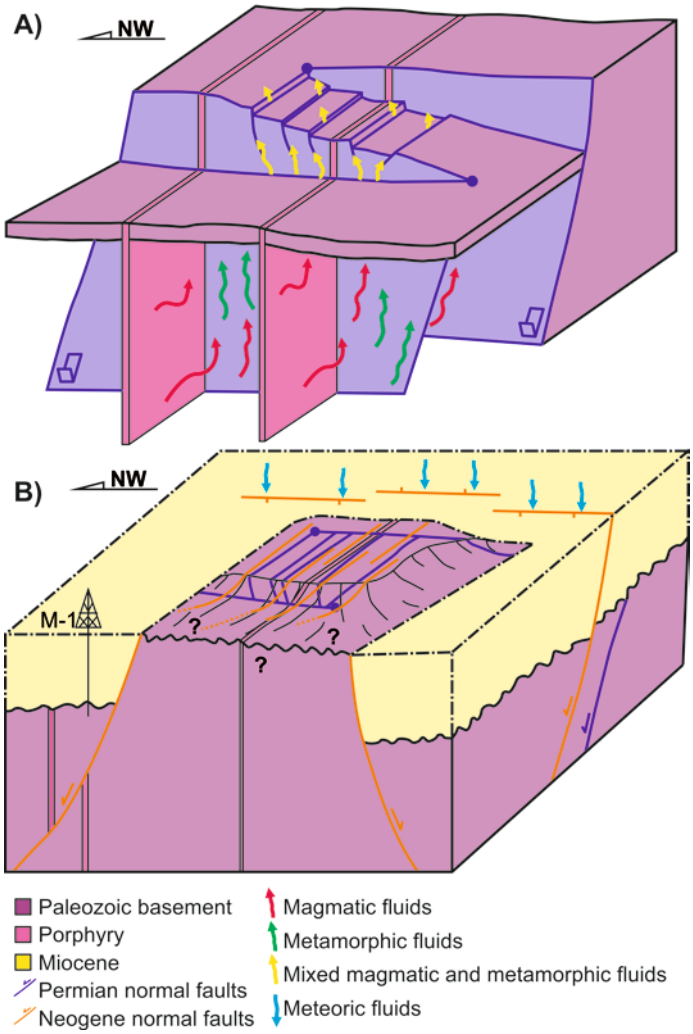
A)
NW
B)
NW
M-1
?
?
?
Paleozoic basement
Porphyry
Miocene
Permian normal faults
Neogene normal faults
Magmatic fluids
Metamorphic fluids
Mixed magmatic and metamorphic fluids
Meteoric fluids

1218